

# Secure Ranging with IEEE 802.15.4z HRP UWB

Xiliang Luo, Cem Kalkanli, Hao Zhou, Pengcheng Zhan, and Moche Cohen  
Apple, California, USA

**Abstract**—Secure ranging refers to the capability of upper-bounding the actual physical distance between two devices with reliability. This is essential in a variety of applications, including to unlock physical systems. In this work, we will look at secure ranging in the context of ultra-wideband impulse radio (UWB-IR) as specified in IEEE 802.15.4z (a.k.a. 4z). In particular, an encrypted waveform, i.e. the scrambled timestamp sequence (STS), is defined in the high rate pulse repetition frequency (HRP) mode of operation in 4z for secure ranging. This work demonstrates the security analysis of 4z HRP when implemented with an adequate receiver design and shows the STS waveform can enable secure ranging. We first review the STS receivers adopted in previous studies and analyze their security vulnerabilities. Then we present a reference STS receiver and prove that secure ranging can be achieved by employing the STS waveform in 4z HRP. The performance bounds of the reference secure STS receiver are also characterized. Numerical experiments corroborate the analyses and demonstrate the security of the reference STS receiver.

**Index Terms**—Secure ranging, impulse radio, UWB, IEEE, 802.15.4z, STS.

## 1. Introduction

Ultra-wideband (UWB) impulse radio (IR) uses a series of short pulses to transmit data. Each pulse in UWB-IR occupies a very small portion of the time in the order of nanoseconds. UWB-IR is ideal for short-range communication between devices, precise ranging and location tracking, and nearby environment sensing [1].

There have been many studies on how to leverage UWB-IR for ranging [2]. Most of the previous work focused on the theoretical limitation of ranging accuracy and sought for optimal ranging solutions with UWB-IR. It was presumed that the receiver could trust the received signal in the sense that there were no adversarial attackers trying to manipulate the ranging waveform. This category of ranging is also referred to as the link-budget optimized ranging [3]. In the meantime, there are many applications which require the integrity of physical ranging to enable various secure transactions. To this end, it is required that the ranging result, i.e., the measured and reported distance, always provides an upper bound on the actual physical distance between two ranging devices, a.k.a. distance-bounding [4], [5], even when adversarial attackers are manipulating the

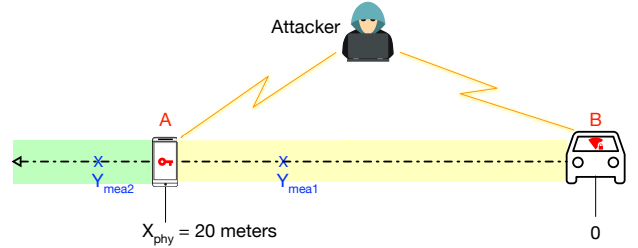


Figure 1. A secure ranging use case. Whenever the measured distance from the phone-key to the car lies within a prescribed interval, e.g. less than 5 meters, the car will open the door according to the protocol. For this protocol to be safe, the phone-key and the car need to ensure that the measured and reported distance is always lower bounded by the actual physical distance even in the presence of an attacker. In other words, the measured distance is always an upper bound on the true physical distance in the case of secure ranging. Distance measurement  $Y_{mea2}$  is a valid one since  $Y_{mea2} > X_{phy}$  and thus causes no security concerns. On the other hand, an attacker will try to reduce the measured distance to  $Y_{mea1}$  such that  $Y_{mea1} < X_{phy}$ .

ranging waveforms exchanged between the ranging devices. This type of ranging is referred to as secure ranging [3], which is the focus of this paper. One example use case of secure ranging is illustrated in Fig. 1.

### 1.1. Prior Work on Secure Ranging

The distance-bounding principle was initially proposed by S. Brands and D. Chaum in [4]. Various distance-bounding protocols were also discussed in [4] while the physical implementations were left as open problems. UWB-IR has been recognized as an ideal candidate to realize secure ranging with distance-bounding since it allows for precise time-of-flight (ToF) measurements thanks to the short impulses in the order of nanoseconds [6]. However, it has been challenging to have a practical UWB-IR system design with provable secure ranging capability. In [7], the authors revealed the vulnerability of the ranging solutions based on the standard IEEE 802.15.4a to distance-decreasing attacks. In particular, the early-decision late-commit (EDLC) attack was employed in [7]. Another type of attack called “Cicada” attack was proposed in [8] to reduce the distance measurement in the receiver designed for 802.15.4a and non-line-of-sight (NLoS) conditions. More studies of physical layer distance-decreasing attacks to 802.15.4a ranging were presented in [9]. Even though 802.15.4a was not ready for secure ranging, the ToF-based distance measurement using UWB-IR was concluded to be the way forward in [10].

Amendment 802.15.4z [11] specified encrypted ranging waveforms to increase the integrity and accuracy of the ranging measurements with respect to 802.15.4a. Ranging security with the low rate pulse repetition frequency (LRP) mode of operation in 4z was studied in [12]. The pulse repetition frequency (PRF) in 4z LRP mode is less than 4 MHz [11]. It was shown that the pulse-reordering modulation scheme was able to secure distance measurement while being robust against all physical-layer distance shortening attacks [12]. Distance-commitment on data is another scheme to achieve distance-bounding with LRP mode of operation by only capturing the energy during the short active radio-frequency (RF) period within each symbol of the data corresponding to the first arriving channel path [11]. In contrast, ranging security is still an open problem in the case of high rate pulse repetition frequency (HRP) mode of operation in 4z with PRF greater than 62 MHz. Due to the higher PRF, the inter-pulse spacing is less than 16 nanoseconds in HRP mode, which is less than the delay spread of typical UWB channels [13] and incurs severe inter-pulse interference. On the other hand, the inter-pulse spacing in LRP mode is more than 250 nanoseconds, which avoids inter-pulse interference and thus allows simple schemes like the distance-commitment on data to achieve ranging security. In [14], the authors provided the first open analysis about the ranging security with the 4z HRP mode. It was claimed that the HRP mode of operation was hard to be configured both secure and of satisfactory detection performance in [14]. In [15], the authors presented over-the-air attacks on several 4z HRP based distance measurement systems and raised concerns about the usage of 4z HRP in security-critical applications.

## 1.2. Main Contributions

The HRP mode in IEEE 802.15.4z has been widely deployed in different solutions [16] due to the hardware implementation advantages associated with the higher PRF. Particularly, since the inter-pulse spacing is less than 16 nanoseconds, a large number of UWB pulses can be transmitted within each millisecond. The requirements on the power amplifier (PA) are thus relaxed. Additionally, the HRP mode is the only one certified by the UWB certification program in Fine Ranging Consortium (FiRa) [17]. However, there have been no published ranging solutions based on 4z HRP establishing the security. In this paper, we demonstrate that secure ranging can be achieved with the STS waveform in 4z HRP mode. Our primary contributions are as follows.

- 1) We characterize all the attack waveforms that are theoretically feasible and provide the rigorous definition of secure ranging in the context of UWB-IR;
- 2) We conduct a review of the previously studied STS receiver for 4z HRP ranging and elucidate why it cannot provide ranging security as noted in [14], [15];
- 3) We present a reference STS receiver design for 4z HRP ranging and prove its security in ensuring the distance-bounding principle. Moreover, the perfor-

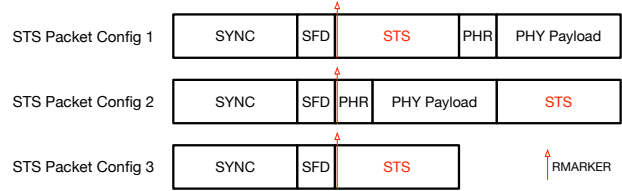


Figure 2. PHY packet formats for ranging integrity in 4z HRP [11].

mance bounds of the reference secure STS receiver are also characterized.

We are witnessing a proliferation of use cases that involve secure ranging. The results in this paper will reinforce the foundation.

## 1.3. Paper Outline

Section 2 provides more details about the HRP mode in IEEE 802.15.4z. Section 3 describes the system model and defines the meanings of “secure ranging” and “feasible attack” in the current context. Section 4 reviews the existing STS receiver design which was widely assumed in previous studies and highlights the effectiveness of one adaptive attack scheme. Section 5 presents a reference ranging receiver design and proves the security together with asymptotic optimality in detection. Performance evaluations are provided in Section 6. Finally, concluding remarks are presented in Section 7.

To facilitate reading, Table 1 and Table 2 in Appendix A list all the key notations, symbols, and acronyms adopted in this paper.

## 2. HRP Mode in IEEE 802.15.4z

Appendix B provides a brief introduction to the standardization of UWB technology since it was approved by FCC in 2002 [18]. The amendment 4z is the focus of the current paper. Note both LRP and HRP modes are defined in IEEE 802.15.4z. The PRF in 4z LRP mode is less than 4 MHz and the inter-pulse spacing is greater than 250 nanoseconds. Yet the PRF is greater than 62 MHz in HRP mode of operation. Accordingly, the inter-pulse spacing is less than 16 nanoseconds. As a result, the UWB pulses in HRP will experience inter-pulse interference (IPI) after propagating through a multi-path channel since the inter-pulse spacing is typically less than the delay spread of the channel [13].

The PHY packet formats specified in 4z HRP for ranging integrity are illustrated in Fig. 2. The designs and functionalities of individual portions in a PHY packet are as follows.

- SYNC (Synchronization): used for initial packet acquisition, timing and frequency synchronization, and channel estimation. In 4z HRP, the SYNC portion includes a repetition of one ternary preamble code that exhibits an ideal periodic auto-correlation, i.e. the delta function;

- SFD (Start-of-Frame Delimiter): used to signal the start of a frame and the end of the SYNC. The SFD in 4z HRP modulates the same ternary code as in SYNC;
- PHR (PHY Header): used for signaling of the PHY payload length;
- PHY Payload: used to convey the data bits from the MAC layer;
- STS (Scrambled Timestamp Sequence): used to enable ranging integrity. The STS portion consists of a sequence of uniformly spaced UWB pulses with pseudo-random polarities that are generated by applying the AES-128 engine in counter mode [19], [20];
- RMARKER (Ranging Marker): defined as the time when the peak of the (hypothetical) pulse associated with the first chip following the SFD is at the local antenna. All reported times during ranging are measured relative to the RMARKER.

Throughout the remainder of this paper, our focus will be on the “STS Packet Config 3” in Fig. 2 and data communication is outside the scope of the current paper.

The inter-pulse spacing between the STS pulses in 4z HRP is either 8 chips for base PRF (BPRF) operation or 4 chips for higher PRF (HPRF) operation with the length of each chip being  $T_c = 1/499.2 \mu\text{s} (\approx 2 \text{ ns})$ . This inter-spacing measured in the unit of chips is also known as the spreading factor (SF).

In 4z HRP mode, the STS portion could be split into multiple segments. The length of each STS segment in time can be expressed as  $T_{\text{sts}} = K_{\text{sts}} \times 512T_c$ , where  $K_{\text{sts}} \in \{16, 32, 64, 128, 256\}$ . Throughout the rest of the paper, we will assume a single STS segment unless stated otherwise.

The higher layer configures the 128-bit STS key. This key is used by the AES-128 engine to generate the cryptographic STS bit sequence consisting of 0’s and 1’s. In 4z HRP, bit 0 corresponds to a positive polarity of +1, while bit 1 corresponds to a negative polarity of -1. Appendix C provides more details about the STS generation structure.

In the SYNC portion, a known preamble code with ideal auto-correlation characteristics is utilized. This design facilitates the initial packet acquisition process and ensures that the system can quickly and accurately establish synchronization. However, it is known that the SYNC is vulnerable to distance-decreasing attacks. For example, an adversary, e.g., the attacker depicted in Fig. 1, could simply transmit the known preamble code at an advanced timing. This will be able to confuse the receiver about the correct arrival time of the ranging packet [9].

In contrast, the attacker cannot predict the STS bit sequence thanks to its cryptographic nature. This is the key property that underpins secure ranging even in the presence of attackers. In Section 5, we will delve into the specifics regarding how the cryptographic STS can be employed for secure ranging.

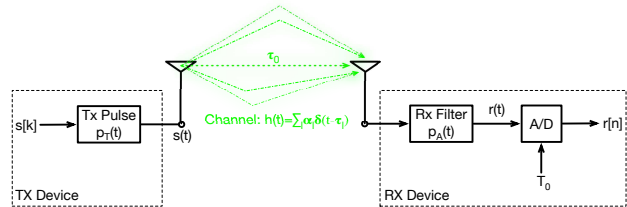


Figure 3. System model for STS-based ranging.

### 3. System Model

In this section, we establish the signal model for the STS-based ranging in 4z HRP. During one exchange of ranging waveform between ranging devices, one transmit-device (TXD) sends a ranging packet to one receive-device (RXD). For example, the phone-key acts as the TXD and the car acts as the RXD in Fig. 1. The ranging packet is formed according to “STS Packet Config 3” in Fig. 2. The RXD receives the ranging packet through a multi-path wireless channel and determines the arrival timing of the first path. More mathematical details regarding this process are given next and Fig. 3 illustrates the overall system.

#### 3.1. STS Waveform from TXD

Let  $p_T(t)$  denote the baseband transmit pulse satisfying<sup>1</sup>  $p_T(t) = 0, \forall t < 0$ . The transmitted STS waveform from the TXD can be expressed as

$$s(t) = \sum_{k=0}^{Q-1} s[k] \cdot p_T(t - k \cdot L \cdot T_c), \quad (1)$$

where  $s[k] \in \{-1, +1\}, k = 0, \dots, Q - 1$ , represents the length- $Q$  bipolar STS sequence,  $L \in \{4, 8\}$  denotes the spreading factor, and  $T_c$  denotes the chip period. Note that  $s(t)$  is the low-pass (a.k.a. baseband) equivalent of the RF signal emitted from the transmit antenna of the TXD<sup>2</sup>.

#### 3.2. Channel Model

As commonly used in UWB literature [13], we also adopt the following multi-path channel model in the baseband:

$$h(t) = \sum_{l \geq 0} \alpha_l \delta(t - \tau_l), \quad (2)$$

where  $\alpha_l$  denotes the complex gain of the  $l$ -th path with a delay of  $\tau_l > 0$  and  $\delta(\cdot)$  is the Dirac delta function. Note  $\tau_0$  is the arrival timing of the first path from the TXD to the RXD.

1. IEEE recommends that the transmitted pulse exhibits minimum precursor energy [11]. In practice, as long as the transmit pulse exhibits a finite support, we can define the earliest timing of non-zero energy as  $t = 0$ .

2. Readers can refer to [21] for more information about the equivalence between the low-pass representation and the corresponding band-pass RF signal.

### 3.3. Received Signal at RXD

After the STS waveform in (1) propagates through the channel in (2), the received baseband signal at the RXD is

$$r(t) = s(t) * h(t) * p_A(t) + w(t), \quad (3)$$

where the operator “\*” stands for the linear convolution operation, filter  $p_A(t)$  captures the overall analog receive filter impulse response, and  $w(t)$  represents the additive noise and interference. Note that  $p_A(t)$  lumps together the effects of the RF front end and the analog front end at the RXD. Meanwhile, causality tells us that  $p_A(t) = 0, \forall t < 0$ . Let  $g(t)$  denote the aggregate received pulse that combines both the multi-path channel in (2) and the overall pulse shape. We have

$$g(t) := p_T(t) * h(t) * p_A(t) = \sum_{l \geq 0} \alpha_l p_R(t - \tau_l), \quad (4)$$

where  $p_R(t) := p_T(t) * p_A(t)$  denotes the aggregate pulse without the channel. It can be seen that  $p_R(t) = 0, \forall t < 0$ . Note  $g(t)$  is referred to as the channel impulse response (CIR) at the RXD<sup>3</sup>. Accordingly, the received signal  $r(t)$  in (3) can be expressed as

$$r(t) = \sum_{k=0}^{Q-1} s[k]g(t - k \cdot L \cdot T_c) + w(t). \quad (5)$$

The received signal in (5) can be further sampled with a time period of  $T_0 = T_c/\Omega$  with  $\Omega$  being an integer greater than or equal to 2 [22]. The resulting digital signal at the RXD is

$$\begin{aligned} r[n] := r(nT_0) &= \sum_{k=0}^{Q-1} s[k]g(nT_0 - k \cdot \Omega L T_0) + w[n], \\ &= \sum_{k=0}^{Q-1} s[k]g[n - kM] + w[n], \end{aligned} \quad (6)$$

where  $g[n] := g(nT_0)$  is the discrete version of the aggregate received pulse,  $M := \Omega L$ , and  $w[n] := w(nT_0)$ .

### 3.4. Secure Ranging Receiver

As the first step in secure ranging, the RXD needs to estimate the first path timing  $\tau_0$  in (2) with the received signal in (6). Let  $\hat{\tau}_0$  denote the estimate. Following the principle of distance-bounding, the RXD further needs to reject this timing estimate whenever it is earlier than the true timing. Before providing a rigorous definition of secure ranging, we need to clarify what kind of attacks to the STS-based ranging are feasible. The following definitions elaborate the meaning of feasible attacks in the context of the ranging system described above.

**Definition 1. (Feasible Attack)** An attack to the STS ranging waveform is feasible only if this attack does not utilize any non-causal information from the cryptographic STS sequence at any time. In other words,  $\forall k$ , at any time within the interval  $((k-1)LT_c, kLT_c)$ , a feasible attack to the STS waveform in (1) can only learn information about

3. The multi-path model in (2) is also termed as channel impulse response sometimes. In this paper, CIR refers to the aggregate pulse shape  $g(t)$ .

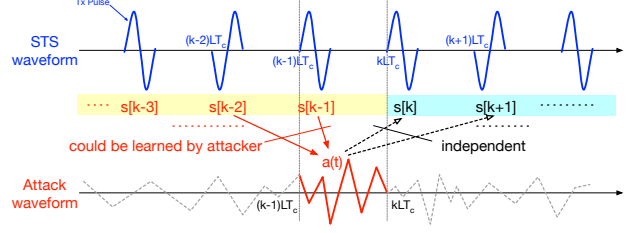


Figure 4. Feasible attacks to STS ranging waveform.

$\{s[n] | n \leq k-1\}$  and is unable to make any inferences about  $\{s[n] | n \geq k\}$ .

An equivalent way to define feasible attacks is as follows.

**Definition 2.** Let  $a(t)$  represent the time-domain attack waveform generated by an attacker. The attack to the STS waveform in (1) is feasible only if  $a(t)$  is independent of  $\{s[n] | n \geq k\}, \forall t < kLT_c$  and  $\forall k$ .

Fig. 4 illustrates feasible attacks according to Definition 2. Next, we provide a precise definition of secure ranging in the current context.

**Definition 3. (Secure Ranging)** The ranging receiver at the RXD is secure only if it ensures that a given estimate of the first path timing  $\eta$  is accepted with a probability no more than a prescribed value whenever it is earlier than  $\tau_0 - \Delta$ , i.e.,

$$\Pr(\text{Accept } \eta | \eta < \tau_0 - \Delta) \leq \rho, \quad (7)$$

where  $\tau_0$  denotes the true timing of the first path,  $\Delta > 0$  is a constant representing the amount of allowed implementation headroom, and  $\rho$  is the prescribed upper bound on the false acceptance rate.

The probability in (7) is with respect to all the random realizations of the STS sequences. Furthermore, this security guarantee also applies to the cases where arbitrary feasible attacks try to advance the timing estimate by manipulating the STS ranging waveform from the TXD.

The above definition builds on the original distance-bounding principle by S. Brands and D. Chaum in [4] while taking into account the physical implementations with UWB-IR. In particular, this definition allows a constant implementation headroom. Taking the use case shown in Fig. 1 as an example, one secure ranging solution shall make sure the measured distance always (or with a probability higher than  $1 - \rho$ ) upper bounds the physical distance as  $X_{\text{phy}} \leq Y_{\text{mea}} + \Delta \cdot c$  with  $c$  denoting the speed of light.

To facilitate a rigorous proof of security, we make the following assumption on the STS sequence  $s[k]$  in (1).

**Assumption 1.** The STS sequence  $\{s[k]\}_{k=0}^{Q-1}$  in (1) is a sequence of independent and identically distributed (IID) binary random variables taking value  $+1$  or  $-1$  with probability 0.5, i.e.,  $\Pr(s[k] = +1) = \Pr(s[k] = -1) = 0.5, \forall k \in [0, Q-1]$ .



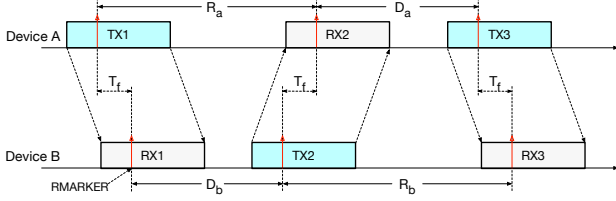


Figure 5. Exchanges of ranging packets in double-sided two-way ranging.

Assumption 1 indeed states the security requirement about the STS sequence as well. Note that the STS key is only shared between two trusted ranging devices through an encrypted logical channel. The attacker has no knowledge of the STS key and can not predict future STS bits by observing the past thanks to the AES construction<sup>4</sup> [14].

We will review different STS receiver designs together with some feasible attacks in Section 4 and Section 5. Furthermore, we will prove the security of the reference STS receiver in Section 5 according to Definition 3.

### 3.5. Clock Frequency Offsets

When two devices perform double-sided two-way ranging (DS-TWR), the packet exchanges and the relevant time measurements are shown in Fig. 5. In particular,  $R_a$  and  $R_b$  denote the ground truth round-trip times while  $D_a$  and  $D_b$  denote the ground truth reply times. Note that all the time measurements are with respect to the corresponding RMARKERS and  $T_f$  represents the time-of-flight (ToF) from Device A to Device B. Also note that the arrival timing of the RMARKER can be inferred from the estimate of the first path timing with the received signal in (6). Due to the clock frequency offsets at both devices, the measured times can be expressed as

$$\hat{R}_a = k_a R_a, \hat{D}_a = k_a D_a, \hat{R}_b = k_b R_b, \hat{D}_b = k_b D_b,$$

where  $k_a$  ( $k_b$ ) denotes the ratio of the clock frequency at Device A (Device B) to the frequency of an ideal clock. As recommended in [11], the ToF can be estimated as

$$\hat{T}_f = (\hat{R}_a \cdot \hat{R}_b - \hat{D}_a \cdot \hat{D}_b) / (\hat{R}_a + \hat{R}_b + \hat{D}_a + \hat{D}_b). \quad (8)$$

Furthermore, it can be shown that the relative error in  $\hat{T}_f$  is only determined by the relative clock offsets [11], i.e.,

$$(\hat{T}_f - T_f) / T_f \approx ((k_a - 1) + (k_b - 1)) / 2. \quad (9)$$

Since both  $(k_a - 1)$  and  $(k_b - 1)$  are in the order of  $\pm 20$  ppm according to the IEEE requirement [11], [25], we see the ranging error due to clock offsets is in the order of pico-second. We can safely neglect this error in practical applications. Accordingly, as the signal model in (6), we

4. The IID property of the STS sequence in the above assumption is based on the premise that only exhaustive key search can break the AES construction [23]. Hoang and Shen recently proved the security and robustness of the random bit generator that runs AES-128 in counter mode in [24].

will assume both the TXD and the RXD have ideal clocks in the sequel.

It is worth mentioning that there is no need to compensate the local clocks at Device A and at Device B to derive the ToF estimate in (8). Similar to the observations in [26], we strongly recommend both Device A and Device B should not try to compensate their local clocks according to the received waveform to avoid potential attacks. Further note that the reference STS receiver presented in Section 5 does not compensate the local clocks.

## 4. CIR Estimation, Thresholding, and Attack

In this section, we first derive the optimal estimate of the CIR based on the received signal model in (6). Then we review the STS receiver that determines the timing of the first path by thresholding the taps in the estimated CIR as in [14], [15]. We further present one feasible attack scheme that can create a fake peak in the CIR at a specified timing. This is distinct from the ‘‘Cicada attack’’ in [8] and the ‘‘random STS attack’’ in [15] (a.k.a. ‘‘ghost peak attack’’) which can only create fake peaks at random locations in the CIR.

### 4.1. CIR Estimation

By resorting to the least-squares principle, the RXD can recover the CIR  $g[n]$  in (6) as in the following proposition. More details can be found in Appendix D.

**Proposition 1.** *Assume the support of  $g[n]$  is limited to  $[0, JM - 1]$ , i.e.,  $g[n] = 0, \forall n \in (-\infty, 0) \cup [JM, +\infty)$ , where  $JM$  characterizes the maximum delay spread of  $g[n]$ . Let  $\mathbf{g}$  denote the vector version of the CIR, i.e.,*

$$\mathbf{g} := [g[0], \dots, g[JM - 1]]^T. \quad (10)$$

*Given the signal model in (6), the RXD can derive the following CIR estimate with the knowledge of  $\{s[k]\}_{k=0}^{Q-1}$ :*

$$\hat{\mathbf{g}} = (\Phi^T \Phi)^{-1} \Phi^T \mathbf{r} := (\Phi^T \Phi / Q)^{-1} \tilde{\mathbf{g}}, \quad (11)$$

where  $\mathbf{r} := [r[0], \dots, r[(Q - 1 + J)M - 1]]^T$ ,  $\tilde{\mathbf{g}} := \Phi^T \mathbf{r} / Q$ , and the matrix  $\Phi$  is a Toeplitz matrix of size  $[(Q - 1 + J)M] \times [JM]$ . Specifically, the first row of  $\Phi$  is given by  $\Phi(1, :) = [s[0], \mathbf{0}_{JM-1}]$  and the first column of  $\Phi$  is given by  $\Phi(:, 1) = [s[0], \mathbf{0}_{M-1}, s[1], \mathbf{0}_{M-1}, \dots, s[Q - 1], \mathbf{0}_{M-1}, \mathbf{0}_{(J-1)M}]^T$ . The notation  $\mathbf{0}_a$  stands for a row vector of all 0's of size 1-by- $a$ .

Note that  $\tilde{\mathbf{g}}$  in (11) represents the intermediate CIR estimate resulting from the simple correlation of the STS sequence with the received signal [14], [15]. To cancel the interference among different CIR taps due to the non-ideal auto-correlation of STS sequence, additional matrix multiplication and inverse operations are performed to derive a cleaner estimate  $\hat{\mathbf{g}}$  as shown in (11).

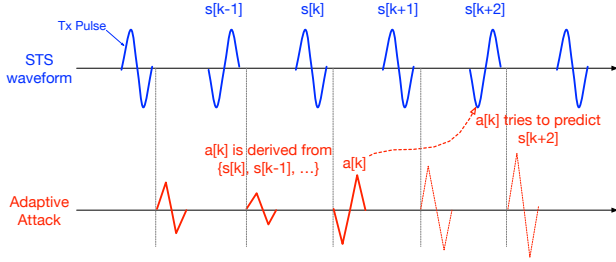


Figure 6. An adaptive scheme to attack the STS waveform.

## 4.2. First Path Validation via CIR Thresholding

In the absence of adversarial attacks, the estimated CIR  $\hat{g}$  according to Proposition 1 will be a superposition of the actual CIR:  $g$  and the estimation error:  $e$ , i.e.,  $\hat{g} = g + e$ . After learning about the standard deviation  $\sigma$  of the samples in  $e$ , one CIR tap could be validated as a true one when the amplitude of the tap exceeds a certain acceptance threshold with respect to the learned standard deviation according to the desired false acceptance rate. One example is illustrated in Fig. 16 in Appendix E where the threshold is set to  $3\sigma$  to realize a false acceptance rate around 0.1% under the Gaussian distribution.

On the other hand, the authors in [14], [15] showed that the estimated CIR could exhibit fake peaks earlier than the true timing of the first path when an adversary attacks the STS waveform. In particular, either the ‘‘Cicada attack’’ in [8] or the ‘‘random STS attack’’ in [15] (a.k.a. ‘‘ghost peak attack’’) could be utilized. Fake early peaks are also illustrated in Fig. 16. It has been recognized that it is hard to configure the acceptance threshold to strike a balance between the false acceptance rate in the case of attacks and the detection performance in validating the true first path when it is weak.

Neither the ‘‘Cicada attack’’ nor the ‘‘random STS attack’’ are able to create fake peaks at given locations in the CIR recovered by the RXD. Next, we will show one particular feasible attack scheme that is able to generate peaks at the designated locations in the CIR based on the targeted distance reduction.

## 4.3. Adaptive Attacking Scheme

In order to create a peak at a designated location in the CIR, one adversary can follow the procedure in Algorithm 1. Although the history STS symbols do not carry any information about the future ones according to Assumption 1, the adversary could try to predict the future STS symbol  $s[k+2]$  by observing the legitimate STS waveform in a causal manner as illustrated in Fig. 6. To this end, the adversary simply updates the empirical estimates of the STS correlation at lags  $\{\Lambda, \Lambda+1, \dots, \Lambda+H\}$  with the observed STS symbol  $s[k]$  as in Step-1 of Algorithm 1.

In Step-2, the adversary exploits these updated empirical estimates of the STS correlation to synthesize the attack

---

### Algorithm 1 Adaptive STS Attack on a Designated CIR Tap

---

1: **INPUT:**

- $\Lambda > 0$ : the step size of empirical prediction;
- $H \geq 0$ : the number of additional history samples utilized during the empirical prediction.

2: **DO** the following steps after learning about the current STS symbol  $s[k]$

- **Step-1:** update the empirical STS correlation value  $\text{corr}[k; \Lambda + \lambda]$ ,  $\lambda \in [0, H]$ , as follows.

$$\text{corr}[k; \Lambda + \lambda] = \sum_{l=\Lambda+H}^k s[l]s[l - \Lambda - \lambda]; \quad (12)$$

- **Step-2:** determine the attack symbol  $a[k]$  as follows.

$$a[k] = \sum_{\lambda=0}^H s[k - \lambda] \cdot \text{corr}[k; \Lambda + \lambda]; \quad (13)$$

- **Step-3:** modulate the pulse with  $a[k]$  and transmit the following attack waveform:

$$a(t) = \sum_{k=0}^{Q-1} a[k] \cdot p_T(t - k \cdot L \cdot T_c). \quad (14)$$

3: **END**

---

symbol  $a[k]$  as in (13). The idea is to utilize the empirical STS correlation at lag  $\Lambda + \lambda$ , i.e.,  $\text{corr}[k; \Lambda + \lambda]$ , to infer information about the future STS symbol  $s[k + \Lambda]$  from the history STS symbol  $s[k - \lambda]$  which has been observed. We have aggregated  $(1 + H)$  inference terms from  $(1 + H)$  history STS samples, i.e.,  $\{s[k - H], s[k - H + 1], \dots, s[k]\}$  in (13). In Fig. 6, the attack symbol  $a[k]$  tries to predict STS symbol  $s[k + 2]$ . The step size of prediction in Fig. 6 is thus  $\Lambda = 2$ .

In Step-3, the adversary transmits the attack waveform by modulating the transmit pulse  $p_T(t)$  with the synthesized attack symbols. Note that we have assumed the adversary employs the same transmit pulse as in (1) to obtain (14). This is for the sake of conciseness in the following derivations. Other pulse shapes are also allowed to realize this adaptive attack.

For the sake of clarity, we assume the attack waveform  $a(t)$  in (14) propagates through a single path channel<sup>5</sup> with gain  $\theta$  and a delay of  $\tau_0$ . Accordingly, the received signal at the RXD becomes

$$r_a(t) = \theta \sum_{k=0}^{Q-1} a[k] p_R(t - k \cdot LT_c - \tau_0). \quad (15)$$

We have neglected the additive noise term in (15). Furthermore, we assume that the legitimate signal is overwhelmed by the attack one. Accordingly, the legitimate signal is also neglected here.

After sampling the signal in (15) with a time period of  $T_0 = T_c/\Omega$  as in (6), we have

$$r_a[n] := r_a(nT_0) = \theta \sum_{k=0}^{Q-1} a[k] p_R[n - kM - \bar{\tau}_0], \quad (16)$$

5. Due to laws of physics, the overall delay of the attack waveform is always lower bounded by the delay of the first path in the channel from the TXD to the RXD for the attacker to learn the STS samples causally.

where  $\tau_0$  is assumed to be an integer multiple of  $T_0$ , i.e.,  $\tau_0 := \bar{\tau}_0 T_0$ , and  $p_R[n] := p_R(nT_0)$ .

Given the received signal in (16), the RXD can recover the CIR according to Proposition 1 as follows.

$$\widetilde{\text{CIR}} = \Phi^T \mathbf{r}_a / Q, \quad (17)$$

$$\widehat{\text{CIR}} = (\Phi^T \Phi / Q)^{-1} \widetilde{\text{CIR}}, \quad (18)$$

where  $\mathbf{r}_a := [r_a[0], \dots, r_a[(Q-1+J)M-1]]^T$ . Now, we can establish the following proposition regarding the adaptive attack scheme in Algorithm 1.

**Proposition 2.** *Let  $\bar{\tau}_0$  denote the actual first path timing in the channel between the attacker and the RXD as in (16). Assume  $p_R(t)$  is confined within  $[0, MT_0)$ . The attack waveform as specified in Algorithm 1 is able to create a peak at  $l_* := (\bar{\tau}_0 + \epsilon - \Lambda M)$ , in the CIR recovered by the RXD as in (18), where  $\epsilon$  could take any integer in  $[0, M-1]$ . Furthermore, the mean value of the tap at  $l_*$  is a multiple of the actual channel gain as  $Q$  gets large, i.e.,*

$$\lim_{Q \rightarrow \infty} \mathbb{E} [\widehat{\text{CIR}}_{l_*}] = -\frac{H+1}{2} \theta \cdot p_R[\epsilon], \quad (19)$$

where the expectation is with respect to the random realizations of the STS sequence under Assumption 1.

Appendix F outlines the proof of the above proposition. Numerical results corroborating the result in (19) are presented in Section 6.1.

#### 4.4. More Discussions

From prior discussions, it is evident that developing a secure ranging capability for an STS receiver is challenging when relying on comparing the taps in the CIR with a particular threshold. Furthermore, an adaptive attack scheme has been presented that can generate a fake peak at a specific location in the CIR. This is due to the fact that the receiver wants to obtain a clean CIR estimate from the received STS ranging waveform. One strong tap could easily overshadow the weak one due to the inter-tap interference. The receiver thus needs to cancel the interference from the strong taps to reveal the weak one. It turns out the interference cancellation process at the receiver could be exploited by the adversary to reduce the distance measurement. It should be noted that the receiver is unaware of whether the received waveform is being manipulated.

We share the same view as in [14], [15] that the simple CIR thresholding based approaches are not recommended for applications where secure ranging is required. However, the encrypted STS ranging waveform in 4z HRP mode of operation is intact. In the following section, we will present a different STS receiver design and prove its security according to Definition 3.

### 5. A Reference STS Receiver with Proved Security

As shown in Proposition 1, the RXD can first obtain an estimate of the CIR after observing the signal  $r[n]$  in (6).

---

#### Algorithm 2 STS Receiver with Proved Security for 4z HRP

---

1: **INPUT:**

- $l_*$ : index of a CIR tap to be validated;
- $\{\hat{r}[n]\}$ : the SYNC samples earlier than the first STS sample that arrives at the timing corresponding to the CIR tap  $l_*$  in the current STS packet;
- $\hat{g}[n]$ ,  $n \in [0, JM-1]$ : the CIR estimate with the SYNC samples  $\{\hat{r}[n]\}$ ;
- $\hat{\beta} > 0$ : a scaling parameter according to the signal power level of the received SYNC samples  $\{\hat{r}[n]\}$ ;
- $\gamma > 0$ : a detection threshold.

2: **DO** the following steps to decide whether the tap  $l_*$  should be accepted or rejected

- **Cancellation:** Cancel the inter-tap interference from  $y[n]$  in (25) with the the CIR estimate  $\hat{g}[n]$ , i.e.,

$$\tilde{x}[n] = y[n] - \sum_{\zeta > 0} \hat{g}[l_* + \zeta M] s[n - \zeta]; \quad (20)$$

- **Saturation:** Scale the signal  $\tilde{x}[n]$  and then input to a non-linear saturation function, i.e.,

$$x[n] = \mathbb{Q} \left( \text{Re} \left\{ \hat{\beta} \cdot \hat{g}[l_*]^\dagger \cdot \tilde{x}[n] \right\} \right), \quad (21)$$

where  $\text{Re}\{\cdot\}$  returns the real part of the argument,  $(\cdot)^\dagger$  is the conjugate operation, and the function  $\mathbb{Q}(\cdot)$  is defined as

$$\mathbb{Q}(x) = \begin{cases} -1 & \text{if } x \leq -1 \\ x & \text{if } x \in (-1, +1) \\ +1 & \text{if } x \geq +1 \end{cases}; \quad (22)$$

- **Validation:** Compute the decision metric as

$$T(\mathbf{x}) = \sum_{n=0}^{Q-1} x[n] s[n] / \sqrt{Q}, \quad (23)$$

and validate CIR tap  $l_*$  according to the following criterion:

$$\begin{cases} \text{Accept } l_* & \text{if } T(\mathbf{x}) \geq \gamma \\ \text{Reject } l_* & \text{if } T(\mathbf{x}) < \gamma \end{cases}, \quad (24)$$

where  $\gamma$  is a threshold.

3: **END**

---

Next the RXD identifies a particular tap in the estimated CIR as the first path candidate and will utilize the corresponding timing to derive the associated ToF value. A critical task here is to either accept this candidate tap as a true physical path or reject it. In the case of attack, there could be fake peaks in the estimated CIR that are earlier than the true physical first path. A secure STS receiver needs to reject any fake peaks earlier than the true first path reliably. Specifically, whenever validating the CIR tap  $l_*$ , the RXD essentially determines one of the following two hypotheses:

$$\begin{aligned}
y[n] := r[l_* + nM] &= \sum_{k=0}^{Q-1} s[k]g[l_* + nM - kM] + w[l_* + nM] = \sum_k g[k]s_e[l_* + nM - k] + w[l_* + nM] \\
&= g[l_*]s[n] + \sum_{\zeta \neq 0} g[l_* + \zeta M]s[n - \zeta] + \dot{w}[n]
\end{aligned} \tag{25}$$

- $\mathcal{H}_0$ : tap  $l_*$  does not correspond to any true physical path;
- $\mathcal{H}_1$ : tap  $l_*$  corresponds to a real physical path.

The probability of accepting  $\mathcal{H}_1$  when  $\mathcal{H}_0$  is true, i.e.,  $\Pr(\mathcal{H}_1; \mathcal{H}_0)$ , dictates the security of the receiver when the candidate tap  $l_*$  is earlier than the true first path. Meanwhile, the probability of deciding  $\mathcal{H}_0$  when  $\mathcal{H}_1$  is true, i.e.,  $\Pr(\mathcal{H}_0; \mathcal{H}_1)$ , characterizes the miss detection rate when a true physical path is indeed present at  $l_*$ .

Following the signal model in (6) and its alternative expression in (44), we can extract the signal samples that convey information about the tap  $l_*$  as in (25), where the first term in (25) comes from the tap  $l_*$ , the second term captures the inter-tap interference,  $\dot{w}[n] := w[l_* + nM]$ , and  $s_e[k]$  denotes the expanded version of  $s[k]$ , i.e.,  $s_e[k] := s[k/M]$ ,  $\forall k = 0, \pm M, \pm 2M, \dots$  and  $s_e[k] = 0$  otherwise.

In the following subsections, we will first present a reference STS receiver and then show how this design guarantees ranging security.

### 5.1. Reference STS Receiver Design

We have illustrated how to validate a given CIR tap  $l_*$  in Algorithm 2. In particular, the RXD first processes the SYNC before utilizing the STS waveform for ranging security. Note the SYNC is ahead of the STS as depicted in Fig. 2. Accordingly, the receiver design in Algorithm 2 makes use of the CIR estimate from the received SYNC. It is worthwhile to mention that the CIR estimate with the SYNC could follow the same principle as in Proposition 1. Specifically, the ideal auto-correlation property of the ternary preamble codes in the SYNC renders  $\Phi^T \Phi \propto \mathbf{I}_{JM}$ , where  $\mathbf{I}_{JM}$  stands for an identity matrix of size  $JM \times JM$ . As a result, the need of matrix inversion in (11) is avoided.

The ‘‘Cancellation’’ step in Algorithm 2 is straightforward according to the signal model in (25). However, unlike conventional designs, only those taps later than tap  $l_*$  are canceled in (20). Albeit minor, this turns out to be an important contribution to the security of the design in Algorithm 2. More analyses will be presented in Section 5.2.

During the step of ‘‘Saturation’’, we first scale the post-cancellation signal before performing the saturation. This is to optimize the detection performance when tap  $l_*$  corresponds to a real physical path while maintaining the specified security level. More details on this will be illustrated in Section 5.4.

The decision metric  $T(x)$  in (23) is compared with a detection threshold  $\gamma$  in the step of ‘‘Validation’’ to make a decision regarding the tap  $l_*$ . This value of this threshold should be configured according to the desired security level as explained in Section 5.2.

### 5.2. Security Analysis

In Section 3.5, we have justified that we can safely assume both the TXD and the RXD have ideal clocks. In the following security analysis, we will first look into the scenario where the clock at the attacker ticks at the same rate as the TXD clock. Section 5.3 will examine how an attacker could take advantage of the clock offsets relative to the TXD.

To analyze the security of the reference STS receiver in Algorithm 2, we can just focus on the case when the CIR tap  $l_*$  is earlier than the first path in (25). When  $l_* < \tau_0/T_0$ , according to (4), we see  $g[l_* + \zeta M] = 0, \forall \zeta \leq 0$ , and  $y[n]$  in (25) becomes

$$y[n] = \dot{w}[n] + y_{\text{legit}}[n], \tag{26}$$

where  $y_{\text{legit}} := \sum_{\zeta > 0} g[l_* + \zeta M]s[n - \zeta]$  and  $\dot{w}[n]$  models both the adversarial attack and the additive noise. According to Definition 2, for any feasible attack, the received waveform from the attacker at time  $n$ , i.e.,  $\dot{w}[n]$  in (26), is independent to the STS sequence starting from time  $n$ , i.e.,  $\{s[k] | k \geq n\}$ . Note the information about  $s[n]$  is only available when the actual first path conveying  $s[n]$  arrives at the RXD. Also note that the legitimate signal  $y_{\text{legit}}[n]$  is also independent of  $\{s[k] | k \geq n\}$ .

Following the steps specified in Algorithm 2, we can verify that the signal after cancellation in (20) and the saturated signal in (21) are both independent of the STS sequence:  $\{s[k] | k \geq n\}$ . Specifically, the estimate of CIR tap  $\hat{g}[n]$  is based on the received SYNC that arrives earlier than the STS. No matter whether the adversary also attacks the SYNC or not, we can see that the tap estimate  $\hat{g}[n]$  from the SYNC is always independent of the STS sequence. Similarly, the scaling parameter  $\hat{\beta}$  is also independent of the STS sequence given that it is determined from the received SYNC as well. Note that the SYNC samples used to estimate  $\hat{g}[n]$  and  $\hat{\beta}$  are those earlier than the first STS sample corresponding to the CIR tap  $l_*$  to be validated. Also note that the SFD in Fig. 2 provides a time gap of more than  $2.9 \mu\text{s}$  between SYNC and STS as specified in 4z [11]. Algorithm 2 makes no assumption regarding whether the SYNC and SFD are under attack or not. We can establish the security of the detector in (24) as follows.

**Proposition 3.** *When validating a CIR tap  $l_*$  that is earlier than the true physical first path, the false acceptance rate of the STS receiver in Algorithm 2 is upper bounded as*

$$\Pr\left(\text{Accept } l_* \mid l_* < \tau_0/T_0\right) \leq \exp(-\gamma^2/2), \tag{27}$$

where the probability is with respect to the random STS sequence under Assumption 1. Meanwhile, the upper bound in (27) is valid under arbitrary feasible attacks.



*Proof.* Let  $T_n := \sum_{k=0}^{n-1} x[k]s[k]$ . We have

$$\begin{aligned} & \mathbb{E}[T_{n+1}|T_n, T_{n-1}, \dots, T_0] \\ &= \mathbb{E}[T_n + x[n]s[n]|T_n, T_{n-1}, \dots, T_0] \\ &= T_n + \mathbb{E}[x[n]s[n]|T_n, T_{n-1}, \dots, T_0] = T_n, \end{aligned} \quad (28)$$

where we have leveraged the independence between  $x[n]$  and  $s[n]$  under arbitrary feasible attacks in obtaining the second equality. From (28), we see the sequence  $\{T_n\}$  is a martingale with bounded increments, i.e.,

$$|T_n - T_{n-1}| \leq 1, \forall n. \quad (29)$$

According to the Azuma-Hoeffding inequality [27], [28] as summarized in Appendix G,  $\forall \epsilon > 0$ , we have

$$\Pr(T_Q \geq \epsilon) \leq \exp\left(-\epsilon^2/2Q\right). \quad (30)$$

The false acceptance rate with the detector in (24) is thus given by

$$\Pr(T(x) \geq \gamma) = \Pr(T_Q \geq \sqrt{Q} \cdot \gamma) \leq \exp(-\gamma^2/2). \quad (31)$$

□

The upper bound in (27) builds the foundation for the security of the STS receiver in Algorithm 2 according to Definition 3. To see this, let  $\eta$  denote the estimate of the first path timing  $\tau_0$  from the CIR  $\hat{g}[n]$ . Various schemes are available to estimate  $\tau_0$  by taking into account the underlying structure of the CIR as in (4), i.e.,  $g(t) = \sum_{l \geq 0} \alpha_l p_R(t - \tau_l)$ . Let  $\chi$  denote the peak timing of the aggregate receive pulse, i.e.,  $\chi := \arg \max_t |p_R(t)|$ . From Proposition 3, we can readily establish the following corollary.

**Corollary 1.** *For a given estimate of the first path timing  $\eta$  and a prescribed upper bound on the false acceptance rate  $\rho$ , we set  $l_* = \lfloor (\eta + \chi)/T_0 \rfloor$  and  $\gamma = \sqrt{2 \ln(1/\rho)}$  in Algorithm 2. Meanwhile, this timing estimate  $\eta$  is accepted only when the tap  $l_*$  is validated as in (24). Accordingly, the probability of false acceptance can be bounded as*

$$\Pr(\text{Accept } \eta | \eta < \tau_0 - \chi) = \Pr(\text{Accept } l_* | l_* T_0 < \tau_0) \leq \rho, \quad (32)$$

where the probability is with respect to the random STS sequence under Assumption 1.

According to Definition 3, the upper bounds on the false acceptance rate in (27) and (32) under arbitrary feasible attacks imply that the STS receiver in Algorithm 2 indeed performs secure ranging with an implementation headroom determined by the pulse shape, i.e.,  $\Delta = \arg \max_t |p_R(t)|$ .

**5.2.1. Uniqueness of UWB-IR.** The fundamental property that enables UWB-IR as an ideal candidate to realize secure ranging is that the pulse width is in the order of nanoseconds. This property makes it possible to realize an implementation headroom as small as several nanoseconds. In particular, for the precursor-free impulse recommended by IEEE in [11], the time distance from the starting to the peak is about 2.5 ns, i.e.,  $\arg \max_t |p_T(t)| \approx 2.5$  ns. Meanwhile, the receiver filter impulse response  $p_A(t)$  could

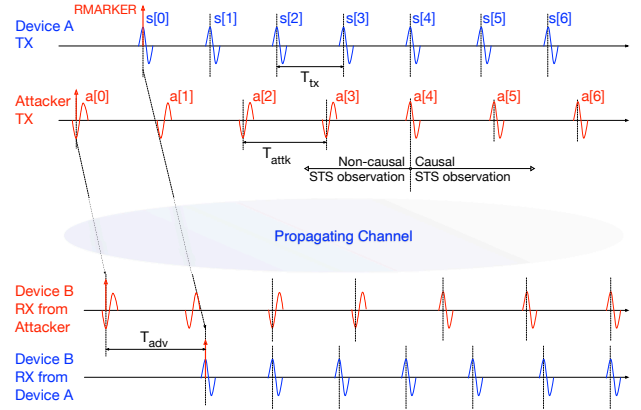


Figure 7. Attack via a slower clock. The inter-pulse spacing from the attacker is larger than that from Device A, i.e.,  $T_{\text{attk}} > T_{\text{tx}}$ . The attacker can advance the RMARKER location at Device B by transmitting the attack sequence earlier than the actual STS sequence from Device A. Due to the slower clock at the attacker, the beginning portion of the attack sequence is independent to the actual STS while the later portion can follow the STS correctly. Specifically, when  $k \geq 4$ , the attacker can follow the STS by listening first and then transmitting, i.e.,  $a(k) = s(k)$ ,  $k \geq 4$ . In this way, the arrival time of the RMARKER is advanced and the corresponding CIR tap could be validated due to the fact that the attack sequence matches the STS partially.

also be designed carefully such that the implementation headroom is minimized. For example, we can limit the headroom to 2.5 ns as well, i.e.,  $\chi = \arg \max_t |p_R(t)| = \arg \max_t |p_T(t) * p_A(t)| \approx 2.5$  ns.

**5.2.2. Special Case with  $\hat{\beta} = \infty$ .** We can look into a special case about the saturation in (21) when the scaling factor  $\hat{\beta}$  is chosen to be  $\infty$ . In this case, the saturated signal in (21) is either  $+1$  or  $-1$ . As the tap  $l_*$  is earlier than the first path, it can be seen that the decision metric in (23) is a summation of IID zero-mean binary random variables. The central limit theorem [28] indicates that the false acceptance rate can be approximated as

$$\Pr(\text{Accept } l_* | l_* < \tau_0/T_0) = \Pr(T(x) \geq \gamma) \approx \mathcal{Q}(\gamma), \quad (33)$$

where  $\mathcal{Q}(\cdot)$  denotes the tail distribution function of the standard normal distribution. It is interesting to recognize that the bound in (27) is indeed the Chernoff bound on  $\mathcal{Q}(\gamma)$ , i.e.,  $\mathcal{Q}(\gamma) \leq \exp(-\gamma^2/2)$ . This further illustrates the general applicability of the result in Proposition 3.

### 5.3. Security under Clock Offset Attack

Although the trusted ranging devices comply with the  $\pm 20$  ppm clock accuracy requirement, an attacker does not need to follow. In fact, an attacker could manipulate its clock offset and try to advance the RMARKER arrival timing. Next we will show how an attacker can advance the RMARKER at the RXD by exploiting a slower clock as in [26]. We will further explain why this is not posing a threat to the security of the STS receiver in Algorithm 2.

When the attacker utilizes the same clock frequency as the TXD, our previous analyses demonstrate that any CIR

tap earlier than the true first path will be rejected subject to a prescribed false acceptance rate. In other words, the attacker cannot advance the arrival timing of the RMARKER at the RXD.

On the other hand, the attacker can exploit a clock slower than the TXD to advance the RMARKER at the RXD. One example of ‘‘Slow Clock Attack’’ is shown in Fig. 7. Let the inter-pulse spacing be  $T_{\text{attk}}$  at the attacker and  $T_{\text{tx}}$  at the TXD. For a length- $Q$  STS sequence, we can define  $T_{\text{adv,max}}$  as

$$T_{\text{adv,max}} := Q(T_{\text{attk}} - T_{\text{tx}}). \quad (34)$$

In order for the attacker to ensure a portion of the attack sequence matches the actual STS from the legitimate TXD, the amount of timing advance of the RMARKER will have to be less than  $T_{\text{adv,max}}$ . Note that the RXD will sync to the attacker’s clock and sample the received waveform in (6) at the clock rate of the attacker when the attacker’s clock ticks differently from that of the TXD. More remarks on the sampling of the received waveform at the RXD are in Appendix H.

The nominal inter-pulse spacing is  $T_{\text{nom}} = LT_c$  with  $L$  being the spreading factor. Consider the  $\pm 20$  ppm requirement on the clock accuracy at both the TXD and the RXD. Meanwhile, we assume that the RXD will reject any input signal that exhibits a relative clock offset beyond  $\Gamma$  ppm with respect to its local clock. Then we can get  $T_{\text{attk}} - T_{\text{tx}} \leq LT_c \cdot (40 + \Gamma)/10^6$ . Note that we typically have  $\Gamma = 40$  in practical implementations to allow maximum interoperability between IEEE devices. Within an STS segment of length  $K_{\text{sts}}$  in the unit of  $512T_c$ , there are  $Q = 512 \cdot K_{\text{sts}}/L$  UWB pulses. Accordingly, we have

$$T_{\text{adv,max}} < K_{\text{sts}} \cdot 512T_c \cdot (40 + \Gamma)/10^6. \quad (35)$$

We see  $T_{\text{adv,max}}$  is proportional to  $K_{\text{sts}}$ . A smaller  $K_{\text{sts}}$  leads to a smaller  $T_{\text{adv,max}}$ . When  $K_{\text{sts}} = 32$  and  $\Gamma = 40$ , we have  $T_{\text{adv,max}} < 2.6$  ns.

By allowing extra implementation headroom in (32), we can establish the security of Algorithm 2 in the presence of clock offsets similar to Corollary 1 as follows.

**Corollary 2.** *For a given estimate of the first path timing  $\eta$  and a prescribed upper bound on the false acceptance rate  $\rho$ , we set  $l_* = \lfloor (\eta + \chi)/T_0 \rfloor$  and  $\gamma = \sqrt{2 \ln(1/\rho)}$  in Algorithm 2. Meanwhile, this timing estimate  $\eta$  is accepted only when the tap  $l_*$  is validated as in (24). Accordingly, the probability of false acceptance can be bounded as*

$$\begin{aligned} & \Pr(\text{Accept } \eta | \eta < \tau_0 - \chi - T_{\text{adv,max}}) \\ &= \Pr(\text{Accept } l_* | l_* T_0 < \tau_0 - T_{\text{adv,max}}) \leq \rho, \end{aligned} \quad (36)$$

where  $\chi := \arg \max_t |p_R(t)|$ ,  $T_{\text{adv,max}} := K_{\text{sts}} \cdot 512T_c \cdot (40 + \Gamma)/10^6$ , and the probability is with respect to the random STS sequence under Assumption 1.

Considering the results in Corollary 1 and Corollary 2, for the sake of clarity in exposition, we will assume the clock at the attacker is ideal as both the TXD and the RXD in this paper unless otherwise specified.

## 5.4. Detection Performance

We next check how well the STS receiver design in Algorithm 2 performs when the CIR tap  $l_*$  corresponds to the true first path in (25). After the interference cancellation step in Algorithm 2, we have

$$\tilde{x}[n] = g[l_*]s[n] + \tilde{w}[n], \quad (37)$$

where  $\tilde{w}[n]$  models both the additive noise and the residual interference from other taps due to non-ideal cancellation.

After the saturation step in (21), we have

$$\begin{aligned} x[n] &= \mathbb{Q} \left( \text{Re} \left\{ \hat{\beta} \cdot \hat{g}[l_*]^\dagger \cdot \tilde{x}[n] \right\} \right) \\ &= \mathbb{Q} \left( \text{Re} \left\{ \hat{\beta} \cdot \hat{g}[l_*]^\dagger (g[l_*]s[n] + \tilde{w}[n]) \right\} \right), \\ &= \mathbb{Q} (\bar{h}s[n] + \bar{w}[n]) \end{aligned} \quad (38)$$

where notation  $(\cdot)^\dagger$  denotes the conjugate operation,  $\bar{h} := \text{Re} \{ \hat{\beta} \cdot \hat{g}[l_*]^\dagger g[l_*] \}$ , and  $\bar{w}[n] := \text{Re} \{ \hat{\beta} \cdot \hat{g}[l_*]^\dagger \tilde{w}[n] \}$ . By defining  $\mathbb{M}(s[n]) := \mathbb{E}[x[n]|s[n]]$ , we have

$$x[n] = \mathbb{M}(s[n]) + e[n], \quad (39)$$

where  $\mathbb{M}(s[n])$  is the conditional mean estimate of  $x[n]$  with  $s[n]$  and  $e[n] := x[n] - \mathbb{M}(s[n])$  stands for the estimation error with a zero mean, i.e.,

$$\mathbb{E}[e[n]] = \mathbb{E}[x[n]] - \mathbb{E}[\mathbb{E}[x[n]|s[n]]] = 0. \quad (40)$$

Further, it can be shown that  $s[n]$  and  $e[n]$  is uncorrelated, i.e.,

$$\begin{aligned} \mathbb{E}[s[n]e[n]] &= \mathbb{E} \left[ \mathbb{E}[s[n] (x[n] - \mathbb{E}[x[n]|s[n]]) | s[n]] \right] \\ &= \mathbb{E} [s[n] \mathbb{E}[x[n]|s[n]] - s[n] \mathbb{E}[x[n]|s[n]]] = 0 \end{aligned} \quad (41)$$

From the decomposition in (39), we can establish the following proposition to characterize the detection performance of the STS receiver in Algorithm 2.

**Proposition 4.** *Assume the estimation error  $e[n]$  in (39) is uncorrelated with  $s[n]$  conditioned on the past samples  $\{x[k]\}_{k < n}$  and the past STS  $\{s[k]\}_{k < n}$ . When validating a CIR tap  $l_*$  corresponding to the true first path, the miss rate of the reference receiver in Algorithm 2 can be upper bounded as*

$$\begin{aligned} \Pr(\text{Reject } l_*) &= \Pr(T(\mathbf{x}) < \gamma) \\ &\leq \exp \left( -Q(\bar{C} - \gamma/\sqrt{Q})^2/2 \right), \end{aligned} \quad (42)$$

where  $C_n := \mathbb{E}[\mathbb{M}(s[n])s[n]]$ ,  $\bar{C} := \sum_{n=0}^{Q-1} C_n/Q$ , and  $\bar{C}\sqrt{Q}$  is large enough such that  $\bar{C} > \gamma/\sqrt{Q}$ . The probability in (42) is with respect to the random STS under Assumption 1.

Appendix I shows the proof outline. Note the condition  $\bar{C} > \gamma/\sqrt{Q}$  can be easily met when the STS length  $Q$  gets large and  $\mathbb{E}[\mathbb{M}(s[n])s[n]] > 0$ . The upper bound in (42) indicates the STS receiver in Algorithm 2 achieves optimal asymptotic detection performance in the sense that

the miss rate decreases to zero exponentially with respect to the STS length. Also note that the correlation value  $C_n = \mathbb{E}[\mathbb{M}(s[n])s[n]]$  can be maximized by optimizing the scaling parameter  $\beta$  in Algorithm 2.

As shown in (41), the estimation error  $e[n]$  is uncorrelated with  $s[n]$ . Besides, the estimation error  $e[n]$  and the current STS sample  $s[n]$  become uncorrelated conditioned on  $\{x[k]\}_{k < n}$  and  $\{s[k]\}_{k < n}$  when the residual term  $\tilde{w}[n]$  in (37) is independent of the past observations and STS. This is the case when the interference cancellation in Algorithm 2 is perfect. The detection performance of one practical implementation with non-ideal interference cancellation will be characterized numerically in Section 6.

## 5.5. More Discussions

Proposition 3 ensures the security of the reference design in Algorithm 2 and Proposition 4 guarantees the detection performance. Compared to the STS receiver based on the simple idea of CIR tap thresholding as reviewed in Section 4, the key factors enabling the security of the reference design can be highlighted as follows.

- When canceling the interference from other CIR taps, it is important to rely on the tap estimates that only utilize the signal arriving earlier than the STS. This is why Algorithm 2 employs the estimated CIR from the SYNC in the packet instead of the STS itself. On the other hand, when canceling the interference on a particular tap with the CIR estimated from the STS, an adversary could exploit this fact and attack the ranging as illustrated in Algorithm 1;
- When canceling the interference from other CIR taps, it is important to only cancel the taps later than the tap being validated. This is why we only cancel the taps at  $l_* + \zeta M$  with  $\zeta > 0$  in (20). Meanwhile, it is worthwhile to point out that the security of the reference design in Algorithm 2 does not necessitate cancellation of all the interfering taps. However, a cleaner signal after cancellation in (20) will lead to improved detection performance;
- The saturation operation in (21) is also critical in establishing the upper bound on the false acceptance rate as in (27) under arbitrary feasible attacks. The contribution from each individual signal sample towards the decision metric in (23) is also restricted by this saturation. Thus the attacker can not achieve extra gains by putting more emphasis on particular signal samples.

In Algorithm 2, we have utilized a particular saturation function as defined in (22), which allows efficient hardware implementation. Note that a different saturation function, e.g., the logistic sigmoid [29], can be employed in the step of ‘‘Saturation’’ without undermining the security of the STS receiver in Algorithm 2.

Also note that the discrete samples in (6) are actually the outputs of the analog-to-digital converter (ADC) at the receiver. Since the ADC outputs are confined within an

interval, the post-cancellation signal in (20) is thus already bounded even without the saturation function  $\mathbb{Q}(\cdot)$  in (22). Accordingly, the security and the upper bound on the false acceptance rate can be established similarly as in Proposition 3. Nevertheless, the ‘‘Saturation’’ step in Algorithm 2 enables optimization of the detection performance.

## 6. Numerical Performance Evaluations

In this section, we corroborate the designs presented in previous sections numerically. In particular, we simulate one HPRF system as illustrated in Fig. 3 with the following configurations:

- STS packet format: STS Packet Config 3 in Fig. 2;
- STS configuration: one STS segment of length  $K_{\text{sts}} = 64$  with spreading factor:  $L = 4$ . The STS sequence length is  $Q = 8192$ ;
- Sampling rate:  $T_0 = T_c/2$  in (6), which corresponds to twice of the chip rate in 4z HRP;
- Receive pulse  $p_R(t)$  in (4): modeled as the precursor-free pulse plotted in Fig. 17 in Appendix J;
- CIR from legitimate TXD to RXD: the channel between legitimate TXD and RXD is modeled as one multi-path channel with the first path corresponding to tap 126 of the length-256 CIR  $g[n]$  in (6), i.e.,  $g[n] = \alpha_0 p_R[n - \bar{\tau}_0] + \sum_{l=1}^{n_{\text{intf}}} \alpha_l p_R[n - \bar{\tau}_l]$ , where  $\alpha_0 = 1$ ,  $\bar{\tau}_0 = 126$ , and  $n_{\text{intf}}$  denotes the number of interfering taps;
- Additive noise: the noise  $w[n]$  in (6) is modeled as AWGN with the variance dictating the signal-to-noise (SNR) ratio at the RXD;
- CIR from attacker to RXD: the channel between the attacker and RXD is modeled as a single tap with  $\theta = 1$  and  $\bar{\tau}_0 = 126$  in (16);
- Timing and frequency synchronization: we assume perfect timing and frequency synchronization at the TXD, the RXD, and the attacker;
- Scaling parameter in the reference STS receiver: we will assume the scaling parameter  $\hat{\beta}$  in Algorithm 2 is set to be  $\infty$ . The saturated signal in (21) is thus simply the sign of the input argument.

### 6.1. Effectiveness of Attack in Algorithm 1

First, we examine the effectiveness of the adaptive attack scheme in Algorithm 1. We neglect the additive noise and assume the legitimate signal is overwhelmed by the attack one. Accordingly, the received signal at the RXD only consists of the adaptive attack signal as in (16). The RXD recovers a CIR estimate of length 256 from the received attack signal according to (11) in Proposition 1. Fig. 8 and 9 depict the statistics about the estimated CIRs over 1000 random STS realizations under different settings of  $\Lambda$  and  $H$  in Algorithm 1. From the statistics, we can see that the adaptive attack is indeed very effective in creating a peak tap at 112. Since  $\Lambda = 2$  and  $M = 8$ , this peak tap is

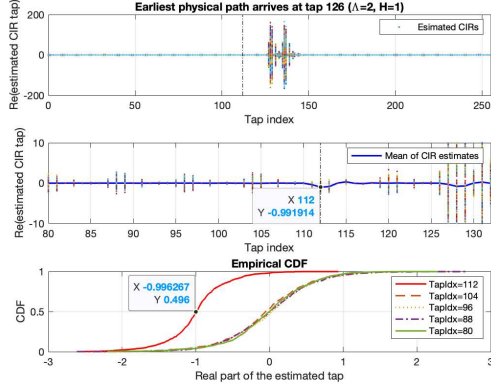


Figure 8. Statistics of CIR estimates under adaptive attacks with  $\Lambda = 2$  and  $H = 1$ .

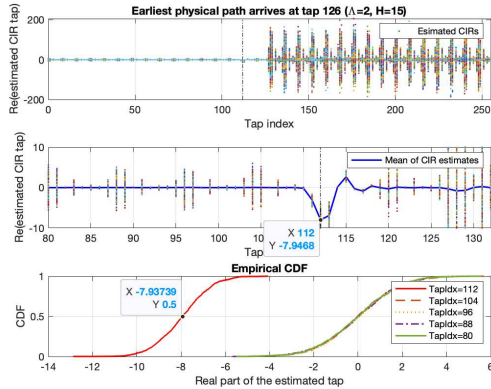


Figure 9. Statistics of CIR estimates under adaptive attacks with  $\Lambda = 2$  and  $H = 15$ .

$\Lambda M = 16$  taps before the peak tap corresponding to the actual first path at 128, which is as predicted in Proposition 2. Meanwhile, we can also see that the amplitude of the early tap at 112 indeed gets larger as we set  $H$  to a higher value in Algorithm 1.

In comparison, Fig. 10 shows the statistics of the CIR estimates when the attacker performs the “ghost peak” attacks as in [15] by transmitting independent random binary sequences. Specifically, the sequence  $\{a[k]\}$  in (15) is a white Bernoulli process with each sample taking the value of  $+10$  or  $-10$  with equal chances. Fig. 10 shows that the “ghost peak” attacks can not ensure an early CIR peak at a prescribed location.

From the above presented results, ones can see that the adaptive attack scheme in Algorithm 1 is effective in generating a fake peak at a specific location in the CIR. On the one hand, it implies those STS receivers that simply compare the amplitudes of the CIR taps against certain thresholds are prone to such attacks. Meanwhile, this also suggests there is no security guarantee to validate one particular CIR tap by comparing the CIR estimate from the SYNC in the packet

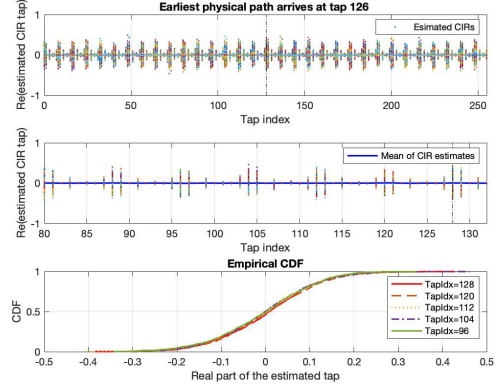


Figure 10. Statistics of CIR estimates under “ghost peak” attacks in [15].

with the one recovered from the STS portion.

## 6.2. Security of STS Receiver in Algorithm 2

Next, we examine the security performance of the reference STS receiver in Algorithm 2. In the absence of attacks, the RXD only receives the legitimate transmission from the TXD as in (6). Fig. 11 shows instances of the estimated CIRs from the received STS signals under different SNR levels. Further, Fig. 12 shows the statistics of the decision metric in (23) when validating CIR taps earlier than the physical first path in the absence of attacks. From the results, we see that the decision metric follows the Gaussian distribution with zero mean and unit variance no matter how strong the noise gets. The desired false acceptance rate of  $\rho$  can be realized by configuring the detection threshold in (24) as  $\gamma = Q^{-1}(\rho)$ .

In the case of the adaptive attack in Algorithm 1, we also employ the reference STS receiver in Algorithm 2 to validate CIR taps earlier than the true physical path. In particular, by setting  $\Lambda = 2$  and  $H = 15$  as in Fig. 9, the statistics of the decision metric in (23) in validating an early CIR tap are shown in Fig. 13. Similarly, Fig. 13 also shows the statistics of the decision metric in (23) in the case of “ghost peak” attacks.

From the above results, we can see that the decision metric in (23) follows the standard normal distribution asymptotically whenever validating non-existing fake taps. Accordingly, the false acceptance probability is always upper bounded as in Proposition 3.

## 6.3. Detection Performance of STS Receiver in Algorithm 2

In this section, we examine the detection performance of the reference STS receiver in Algorithm 2 in the absence of attacks. In particular, the received signal at the RXD consists of the legitimate STS waveform from the TXD and the AWGN as in (6). With the same CIR configuration as in Fig. 11, we next present the detection performance



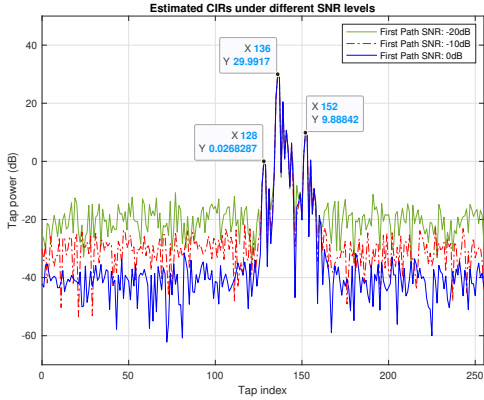


Figure 11. CIR estimates from the STS signals under different SNRs without attacks ( $n_{\text{intf}} = 3$ ,  $(\alpha_0, \bar{\tau}_0) = (0\text{dB}, 126)$ ,  $(\alpha_1, \bar{\tau}_1) = (30\text{dB}, 134)$ ,  $(\alpha_2, \bar{\tau}_2) = (0\text{dB}, 142)$ ,  $(\alpha_3, \bar{\tau}_3) = (10\text{dB}, 150)$ ).

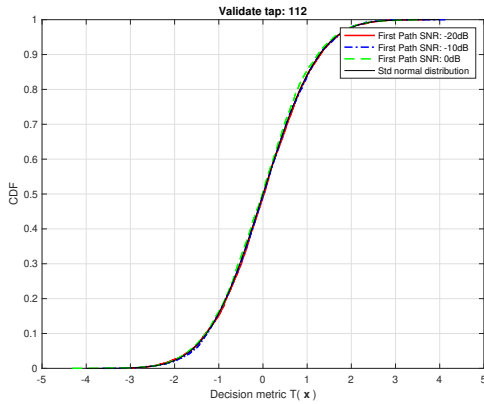


Figure 12. CDFs of the decision metric when validating the CIR tap 112 in the absence of attacks.

when validating the tap of  $l_* = 128$ , which corresponds to the pulse peak on the first path. Note that we have  $\arg \max_n |p_R[n]| = 2$  and  $\bar{\tau}_0 = 126$ . Fig. 14 shows the detection performance of the first path when the detection threshold in (24) is set to  $\gamma = Q^{-1}(10^{-6})$  to ensure the false acceptance rate at  $10^{-6}$ . Note that the inter-tap interference cancellation in (20) may be non-ideal either due to the errors in the estimates of the interference taps or simply because we do not cancel all of the interference taps. Fig. 14 also depicts the detection performance with different amount of residual inter-tap interference. The results indicate that the detection performance does not degrade much without canceling those interference taps that are less than 10dB with respect to the first path.

Fig. 14 also shows the corresponding detection performance when targeting different false acceptance rates, i.e.,  $\rho = 10^{-6}$ ,  $2^{-30}$ , and  $2^{-48}$ . To gain a higher level of security with a smaller false acceptance rate, we need to set a higher detection threshold in Algorithm 2. The detection performance thus degrades accordingly. Note that the target

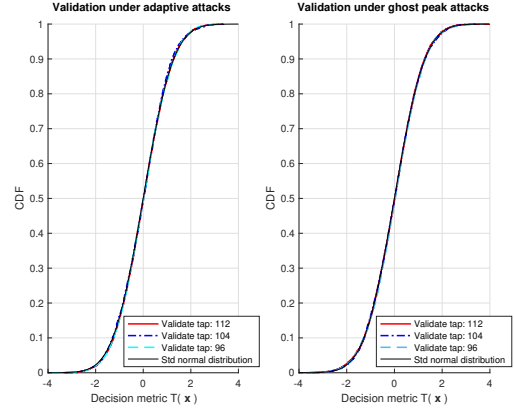


Figure 13. CDFs of the decision metric when validating different CIR taps in the case of attacks. Left: adaptive attacks with  $\Lambda = 2$  and  $H = 15$ . Right: “ghost peak” attacks.

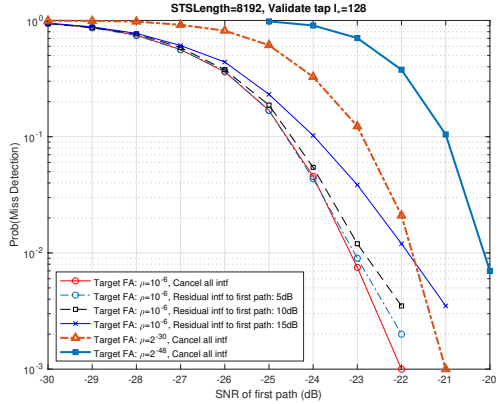


Figure 14. Miss detection performance with a target false acceptance rate of  $\rho = 10^{-6}$ ,  $2^{-30}$ ,  $2^{-48}$ . “Cancel all intf”: all the interference from taps at 136, 144, and 152 are canceled; “Residual intf to first path:  $x$ dB”: the amount of interference after cancellation is  $x$  dB over the first path power.

false rates of  $10^{-6}$  and  $2^{-48}$  correspond to the medium and high security levels in FiRa certification [17] respectively. While ensuring the false acceptance rate of  $2^{-48}$ , Fig. 14 shows that the reference STS receiver in Algorithm 2 can detect the first path with a probability more than 99% as long as the SNR of the first path is above  $-20\text{dB}$ .

## 7. Conclusions

In this paper, we have presented a reference STS receiver and demonstrated that secure ranging can be achieved by employing the STS waveform in 4z HRP. We have also characterized the performance bounds of the reference secure STS receiver.

On one hand, the results in this paper address all the concerns about the security of 4z HRP mode. On the other hand, the reference STS receiver and the highlighted design principles in this paper will fortify the foundation for all the use cases building on secure ranging with 4z HRP UWB.

## References

- [1] M.-G. D. Benedetto, T. Kaiser, A. F. Molish, I. Oppermann, C. Politano, and D. Porcino, *UWB Communication Systems: A Comprehensive Overview*. New York, NY, USA: Hindawi Publishing Corporation, 2006.
- [2] Z. Sahinoglu, S. Gezici, and I. Guvenc, *Ultra-wideband Positioning Systems: Theoretical Limits, Ranging Algorithms, and Protocols*. Cambridge, UK: Cambridge University Press, 2008.
- [3] G. Mandyam, X. Luo, and E. Perraud, "UWB Secure Ranging in FiRa," *FiRa Consortium*, August 2022.
- [4] S. Brands and D. Chaum, "Distance-bounding protocols," in *Proc. EUROCRYPT'93, Lecture Notes in Computer Science 765*, Springer, 1993, pp. 344–359.
- [5] G. Avoine, M. A. Bingol, I. Boureanu, S. Capkun, G. Hancke, S. Kardas, C. H. Kim, C. Lauradoux, B. Martin, J. Munilla, A. Peinado, K. B. Rasmussen, D. Singelee, A. Tchamkerten, R. Trujillo-Rasua, and S. Vaudenay, "Security of distance-bounding: A survey," *ACM Computing Surveys*, vol. 51, no. 5, pp. 1–33, September 2018.
- [6] G. Hancke and M. Kuhn, "An RFID distance bounding protocol," in *Proceedings of 1st International Conference on Security and Privacy for Emerging Areas in Communications Networks (SECURECOMM'05)*, Athens, Greece, September 5-9 2005, pp. 67–73.
- [7] M. Flury, M. Poturalski, P. Papadimitratos, J.-P. Hubaux, and J.-Y. Le Boudec, "Effectiveness of distance-decreasing attacks against impulse radio ranging," in *Proceedings of the 3rd ACM Conference on Wireless Network Security (WiSec'10)*, Hoboken, NJ, USA, March 22-24 2010, p. 117–128.
- [8] M. Poturalski, M. Flury, P. Papadimitratos, J.-P. Hubaux, and J.-Y. Le Boudec, "The cicada attack: Degradation and denial of service in IR ranging," in *Proceedings of 2010 IEEE International Conference on Ultra-Wideband*, Nanjing, China, September 20-23 2010, pp. 1–4.
- [9] —, "Distance bounding with IEEE 802.15.4a: Attacks and countermeasures," *IEEE Transactions on Wireless Communications*, vol. 10, no. 4, pp. 1334–1344, April 2011.
- [10] A. Ranganathan and S. Capkun, "Are we really close? Verifying proximity in wireless systems," *IEEE Security & Privacy*, vol. 15, no. 3, pp. 52–58, June 2017.
- [11] *IEEE Standard for Low-Rate Wireless Networks - Amendment 1: Enhanced Ultra Wideband (UWB) Physical Layers (PHYs) and Associated Ranging Techniques*, IEEE Std. 802.15.4z, 2020.
- [12] M. Singh, P. Leu, and S. Capkun, "UWB with pulse reordering: Securing ranging against relay and physical-layer attacks," in *Proceedings of Network and Distributed Systems Security (NDSS) Symposium*, San Diego, CA, USA, February 24 - 27 2019, pp. 1–15.
- [13] A. F. Molisch, "Ultra-wide-band propagation channels," *Proceedings of the IEEE*, vol. 97, no. 2, pp. 353–371, February 2009.
- [14] M. Singh, M. Roeschlin, E. Zalzal, P. Leu, and S. Capkun, "Security analysis of IEEE 802.15.4z/hrp uwb time-of-flight distance measurement," in *Proceedings of the 14th ACM Conference on Security and Privacy in Wireless and Mobile Networks (WiSec'21)*, Abu Dhabi, United Arab Emirates, June 28 - July 2 2021, pp. 227–237.
- [15] P. Leu, G. Camurati, A. Heinrich, M. Roeschlin, C. Anliker, M. Hollick, S. Capkun, and J. Classen, "Ghost peak: Practical distance reduction attacks against hrp uwb ranging," in *Proceedings of the 31st USENIX Security Symposium*, Boston, MA, USA, August 10 - 12 2022, pp. 1343–1359.
- [16] D. Coppens, A. Shahid, S. Lemey, B. Van Herbruggen, C. Marshall, and E. De Poorter, "An overview of uwb standards and organizations (IEEE 802.15.4, FiRa, Apple): Interoperability aspects and future research directions," *IEEE Access*, vol. 10, pp. 70 219–70 241, June 2022.
- [17] *FiRa Consortium - FiRa Certification Program*, 2023. [Online]. Available: <https://www.firaconsortium.org>
- [18] *FCC First Report and Order: In the Matter of Revision of Part 15 of the Commission's Rules Regarding Ultra-Wideband Transmission Systems*, Federal Communications Commission, FCC 02-48, April 2002.
- [19] *Announcing the Advanced Encryption Standard (AES)*, United States National Institute of Standards and Technology (NIST), Federal Information Processing Standards Publication 197, November 2001.
- [20] *Recommendation for Random Number Generation Using Deterministic Random Bit Generators*, United States National Institute of Standards and Technology (NIST), NIST Special Publication 800-90A Revision 1, June 2015.
- [21] J. G. Proakis and M. Salehi, *Digital Communications*, 5th ed. New York, NY, USA: McGraw-Hill, 2007.
- [22] A. Oppenheim and R. Schaffer, *Discrete-Time Signal Processing*, 3rd ed. Upper Saddle River, New Jersey, USA: Pearson, 2009.
- [23] J. Katz and Y. Lindell, *Introduction to Modern Cryptography*, 3rd ed. Boca Raton, FL, USA: CRC Press, 2021.
- [24] V. T. Hoang and Y. Shen, "Security analysis of NIST CTR-DRBG," in *Advances in Cryptology - CRYPTO 2020*, D. Micciancio and T. Ristenpart, Eds. Cham: Springer International Publishing, August 17-21 2020, pp. 218–247.
- [25] *IEEE Standard for Low-Rate Wireless Networks*, IEEE Std. 802.15.4, 2020 (Note: Amendment IEEE 802.15.4a has been merged into this version as Chapter 14 and 15).
- [26] C. Anliker, G. Camurati, and S. Capkun, "Time for change: How clocks break uwb secure ranging," in *Proceedings of the 32nd USENIX Security Symposium*, Anaheim, CA, USA, August 9 - 11 2023, pp. 19–36.
- [27] W. Hoeffding, "Probability inequalities for sums of bounded random variables," *Journal of the American Statistical Association*, vol. 58, no. 301, p. 13–30, March 1963.
- [28] G. Grimmett and D. Stirzaker, *Probability and Random Processes*, 3rd ed. Great Clarendon Street, Oxford, UK: Oxford University Press, 2001.
- [29] I. Goodfellow, Y. Bengio, and A. Courville, *Deep Learning*. Cambridge, MA, USA: The MIT Press, 2016.
- [30] J. del Prado Pavon, S. Shankar N, V. Gaddam, K. Challapali, and C.-T. Chou, "The MBOA-WiMedia specification for ultra wideband distributed networks," *IEEE Communications Magazine*, vol. 44, no. 6, pp. 128–134, June 2006.
- [31] R. Fisher, R. Kohno, H. Ogawa, H. Zhang, M. McLaughlin, and M. Welborn, "DS-UWB physical layer submission to 802.15 task group 3a," *IEEE P802.15-04/0137r4*, 2005.

## Appendix A.

### Key Notations, Symbols, and Acronyms

All the key notations and symbols adopted in this paper are listed in Table 1 together with corresponding definitions. The acronyms used in this paper are listed in Table 2.

## Appendix B.

### UWB Standardization

The Federal Communications Commission (FCC) in the United States authorized the use of UWB for commercial purposes in 2002 [18]. The first UWB standard was proposed by the MultiBand OFDM Alliance (MBOA) in 2004 and took a wideband orthogonal frequency-division multiplexing (OFDM) approach [30]. Meanwhile, an IR-based proposal was put forward by the WiMedia Alliance,

TABLE 1. LIST OF SYMBOLS AND NOTATIONS

Symbol	Definition (Typical Values)
$T_c$	Chip duration ( $= 1/499.2 \mu\text{s}$ , $\approx 2 \text{ ns}$ )
$T_0$	Sampling period ( $T_0 = T_c/\Omega$ , $\Omega \geq 2$ )
$\{s[k]\}_{k=0}^{Q-1}$	Length- $Q$ STS sequence ( $s[k] = \pm 1$ , $Q = 8192$ )
$L$	Spreading factor ( $L \in \{4, 8\}$ )
$s(t)$	Transmitted STS waveform in the baseband from TXD
$T_{\text{sts}}$	Length of one STS segment
$K_{\text{sts}}$	Length of one STS segment in the unit of $512T_c$ , i.e., $T_{\text{sts}} = K_{\text{sts}} \times (512T_c)$ ( $K_{\text{sts}} = 64$ )
$p_T(t)$	Transmit impulse in the baseband
$p_A(t)$	Receiver analog front-end filter impulse response
$p_R(t)$	Aggregate receive pulse shape without channel
$\chi$	Peak timing of the receive pulse, i.e., $\chi = \arg \max_t  p_R(t) $ ( $2.5 \text{ ns}$ )
$h(t)$	Multi-path channel model
$\alpha_l$	The complex magnitude of the $l$ -th path in $h(t)$
$\tau_l$	The time delay of the $l$ -th path in $h(t)$
$g(t); g[n]$	Aggregate pulse shape with channel, a.k.a. CIR; $g[n] = g(nT_0)$
$r(t); r[n]$	Received signal at RXD; $r[n] = r(nT_0)$
$\eta$	Estimate of the arrival timing of the first path
$\Delta$	Allowed implementation headroom in secure ranging
$\rho$	Prescribed upper bound on the false acceptance rate ( $\rho = 2^{-48}$ )
$T_f; \hat{T}_f$	ToF between ranging devices; the ToF estimate
$\Lambda$	A positive integer-valued step size of empirical prediction in adaptive STS attack ( $\Lambda \in \mathbb{Z}^+$ )
$H$	Number of additional history samples used for empirical prediction ( $H \in \mathbb{Z}^+ \cup \{0\}$ )
$\{a[k]\}_{k=0}^{Q-1}$	Attack symbols in adaptive STS attack
$a(t)$	Waveform of adaptive STS attack
$\theta$	Path gain of the channel from the attacker to RXD
$\bar{\tau}_l$	The discrete value of $\tau_l$ when $\tau_l = \bar{\tau}_l T_0$
$\{\hat{g}[n]\}_{n=0}^{JM-1}$	CIR estimate with the SYNC in the current STS packet
$\hat{\beta} > 0$	Scaling parameter configured according to the received signal power level over SYNC
$l_*$	Index of the tap to be validated in the CIR $\hat{g}[n]$
$T(\mathbf{x})$	Decision metric to validate a given CIR tap
$\gamma$	Detection threshold to accept a given CIR tap
$\Gamma$	Maximum relative clock offset in ppm allowed by RXD ( $\Gamma = 40 \text{ ppm}$ )
$\mathcal{Q}(\cdot)$	Tail distribution function of the standard normal distribution, a.k.a. Q-function
$\Pr(\cdot)$	Probability of the specified event
$E[\cdot]$	Expectation of the specified random variable
$\mathbf{A}(i, j)$	The element of matrix $\mathbf{A}$ at the intersection of the $i$ -th row and the $j$ -th column
$\mathbf{A}(i, :)$	The $i$ -th row vector of matrix $\mathbf{A}$
$\mathbf{A}(:, j)$	The $j$ -th column vector of matrix $\mathbf{A}$

which used a direct-sequence UWB (DS-UWB) approach [31]. IEEE 802.15.4 [25] is a wireless networking standard that specifies the physical layer (PHY) and medium access control (MAC) sublayers for a low-rate wireless personal area network (LR-WPAN). In 2006, an amendment to the standard, IEEE 802.15.4a, added a new PHY based on UWB-IR to provide higher precision ranging and localization capability and higher aggregate throughput.

In 2017, the IEEE 802.15 working group initiated efforts to define a series of PHY enhancements to improve the capabilities of UWB devices. In 2018, the task group 802.15.4z started to work on the corresponding amendment

TABLE 2. LIST OF ACRONYMS

Acronym	Full-form Meaning
UWB-IR	ultra-wideband impulse radio
ToF	time-of-flight
LRP	low rate pulse repetition frequency
HRP	high rate pulse repetition frequency
PRF	pulse repetition frequency
BPRF	base pulse repetition frequency
HPRF	higher pulse repetition frequency
PHY	physical layer
SYNC	synchronization
SFD	start-of-frame delimiter
STS	scrambled timestamp sequence
SF	spreading factor
RMARKER	ranging marker
TXD	transmit-device
RXD	receive-device
DS-TWR	double-sided two-way ranging
CIR	channel impulse response

to IEEE 802.15.4. This amendment, i.e., IEEE 802.15.4z [11], was completed and published in 2020. Amendment 4z enhanced the UWB PHYs and associated ranging techniques. In particular, amendment 4z specified encrypted ranging waveforms to increase the integrity and accuracy of the ranging measurements. A more comprehensive overview of UWB standards and organizations is available in [16].

## Appendix C. STS Generation DRBG

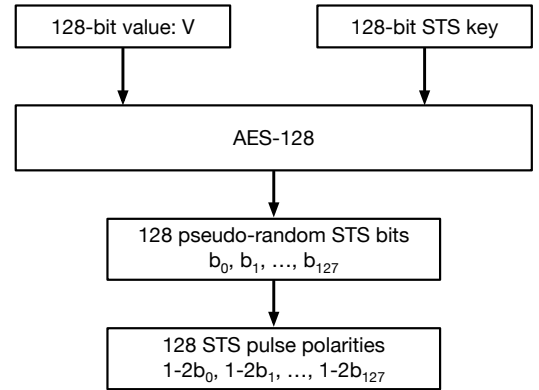


Figure 15. STS generation with AES-128 in counter mode.

The deterministic random bit generator (DRBG) [20] for generation of STS bits is specified by IEEE in [11] and is depicted in Fig. 15. This DRBG produces 128 pseudo-random STS bits after each run. The higher layer is responsible for setting the 128-bit STS key and the 128-bit initial value for  $V$ . The value of  $V$  is incremented after each run of the DRBG and outputting 128 bits. In this way, fresh STS bits are generated for each STS packet.

IEEE also recommends that re-seeding should be carried out when specific levels of backtracking resistance are required or a large number of iterations are performed.

## Appendix D. Proof of Proposition 1

*Proof.* We can re-write the received signal in (6) as

$$r[n] = \sum_{k=0}^{(Q-1)M} s_e[k]g[n-k] + w[n], \quad (43)$$

$$= \sum_{k=0}^{JM-1} g[k]s_e[n-k] + w[n], \quad (44)$$

where  $s_e[k]$  is an expanded version of  $s[k]$ , i.e.,  $s_e[k] = s[k/M]$ ,  $\forall k = 0, \pm M, \pm 2M, \dots$  and  $s_e[k] = 0$  otherwise, and the second equality is due to the commutative property of the linear convolution operation.

By utilizing the vector notation as defined in Proposition 1, the signal model in (44) can be further expressed as

$$\mathbf{r} = \Phi \mathbf{g} + \mathbf{w}, \quad (45)$$

where  $\mathbf{w} := [w[0], \dots, w[(Q-1+J)M-1]]^T$ . The least-squares solution to the linear system in (45) can be obtained as in (11), i.e.,

$$\hat{\mathbf{g}} = (\Phi^T \Phi)^{-1} \Phi^T \mathbf{r}. \quad (46)$$

Note that the least-squares solution is indeed the maximum-likelihood one when the noise vector  $\mathbf{w}$  is white Gaussian.  $\square$

## Appendix E. CIR Thresholding

One CIR tap could be validated as a true one when the amplitude of the tap exceeds a certain acceptance threshold with respect to the learned standard deviation according to the desired false acceptance rate. In Fig. 16, the threshold is set to  $3\sigma$  to realize a false acceptance rate around 0.1% under the Gaussian distribution. On the other hand, fake peaks can show up earlier than the true first path in the presence of attacks.

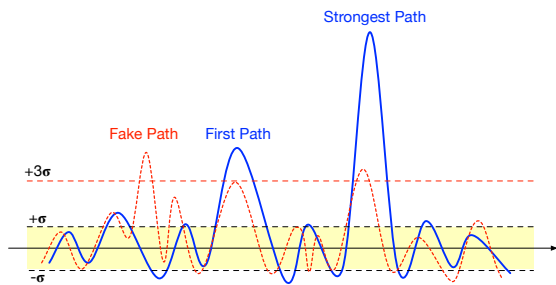


Figure 16. Solid **Blue**: estimated CIR in the absence of adversarial attacks. Dotted **Red**: CIR with fake peaks in the presence of attacks as in [14], [15]. The standard deviation of the estimation errors is  $\sigma$ .

## Appendix F. Proof of Proposition 2

*Proof.* Among all the received signal samples in (16), we can focus on the following set of signal samples that convey information about the tap  $l_* = \bar{\tau}_0 + \epsilon - \Lambda M$ :

$$y[n] := r_a[l_* + nM] = \theta \sum_k p_R[k - \bar{\tau}_0] a_e[l_* + nM - k], \quad (47)$$

where  $a_e[k]$  the expanded version of  $a[k]$ , i.e.,  $a_e[k] = a[k/M]$  when  $k$  is a multiple of  $M$  and  $a_e[k] = 0$  otherwise. Considering  $\epsilon \in [0, M-1]$ , we can further simplify  $y[n]$  in (47) as

$$\begin{aligned} y[n] &= \theta \sum_{k, k=l_*+jM} p_R[k - \bar{\tau}_0] a_e[l_* + nM - k] \\ &= \theta \sum_j p_R[l_* + jM - \bar{\tau}_0] a_e[(n-j)M] \\ &= \theta \sum_j p_R[(j-\Lambda)M + \epsilon] a[n-j] \\ &= \theta \cdot p_R[\epsilon] \cdot a[n-\Lambda], \end{aligned} \quad (48)$$

where we have utilized the assumption that  $p_R(t)$  is confined within the time interval of  $[0, MT_0)$  to get the last equality.

With the observations  $\{y[n]\}$  in (48), the RXD first obtains an initial estimate of the CIR tap at  $l_* + \zeta M$ ,  $\zeta \geq 0$ , according to (17) as

$$\widetilde{\text{CIR}}_{l_* + \zeta M} = \frac{1}{Q} \sum_{n=0}^{Q-1} s[n - \zeta] \cdot y[n]. \quad (49)$$

Note that  $s[n] = 0$  when  $n < 0$ . In particular, after substituting  $y[n]$  with (48) and following the definition of attack in (13), the estimate of the CIR tap at  $l_* + (\Lambda + \lambda)M$  can be found in (50).

To refine the CIR estimate in (50), interference cancellation can be performed as in (18). As the first-order approximation to the matrix inversion in (18), we have

$$(\Phi^T \Phi / Q)^{-1} = (\mathbf{I}_{JM} + \Delta)^{-1} \approx \mathbf{I}_{JM} - \Delta, \quad (51)$$

where  $\mathbf{I}_{JM}$  denotes the  $JM \times JM$  identity matrix and  $\Delta$  captures the off-diagonal autocorrelation of the STS sequence. Specifically, we have  $\Delta(i, i) = 0$  and  $\Delta(i, i+j) = \sum_k s_e[k]s_e[k-j]/Q$  when  $j \neq 0$ , where  $s_e[k]$  is defined as in (44). According to the above approximation, we can cancel the interference to CIR tap at  $l_*$  as

$$\begin{aligned} \widetilde{\text{CIR}}_{l_*} &= \frac{1}{Q} \\ &\sum_{n=0}^{Q-1} s[n] \cdot \left( y[n] - \sum_{\lambda \neq -\Lambda} s[n - \Lambda - \lambda] \cdot \widetilde{\text{CIR}}_{l_* + (\Lambda + \lambda)M} \right) \\ &= \widetilde{\text{CIR}}_{l_*} - \sum_{\lambda \neq -\Lambda} \sum_{n=0}^{Q-1} \frac{\widetilde{\text{CIR}}_{l_* + (\Lambda + \lambda)M}}{Q} s[n] s[n - \Lambda - \lambda]. \end{aligned} \quad (52)$$



$$\begin{aligned}
& \widetilde{\text{CIR}}_{l_* + (\Lambda + \lambda)M} \\
&= \frac{\theta \cdot p_R[\epsilon]}{Q} \sum_{n=0}^{Q-1} s[n - \Lambda - \lambda] \cdot a[n - \Lambda] = \frac{\theta \cdot p_R[\epsilon]}{Q} \sum_{n=0}^{Q-1} s[n - \Lambda - \lambda] \cdot \left( \sum_{\lambda'=0}^H s[n - \Lambda - \lambda'] \sum_{l=\Lambda+H}^{n-\Lambda} s[l]s[l - \Lambda - \lambda'] \right) \\
&= \frac{\theta \cdot p_R[\epsilon]}{Q} \sum_{\lambda'=0}^H \sum_{n=0}^{Q-1} \sum_{l=\Lambda+H}^{n-\Lambda} s[n - \Lambda - \lambda]s[n - \Lambda - \lambda'] \cdot s[l]s[l - \Lambda - \lambda']
\end{aligned} \tag{50}$$

$$\begin{aligned}
\mathbb{E} \left[ \widehat{\text{CIR}}_{l_*} \right] &= -\frac{\theta \cdot p_R[\epsilon]}{Q^2} \cdot \sum_{\lambda \neq -\Lambda} \mathbb{E} \left[ \sum_{n=0}^{Q-1} s[n]s[n - \Lambda - \lambda] \sum_{\lambda'=0}^H \sum_{n'=0}^{Q-1} \sum_{l=\Lambda+H}^{n'-\Lambda} s[n' - \Lambda - \lambda]s[n' - \Lambda - \lambda']s[l]s[l - \Lambda - \lambda'] \right] \\
&= -\frac{\theta \cdot p_R[\epsilon]}{Q^2} \cdot \sum_{\lambda=0}^H \mathbb{E} \left[ \sum_{n=0}^{Q-1} s[n]s[n - \Lambda - \lambda] \sum_{n'=0}^{Q-1} \sum_{l=\Lambda+H}^{n'-\Lambda} s[l]s[l - \Lambda - \lambda] \right] \\
&= -\frac{\theta \cdot p_R[\epsilon]}{Q^2} \cdot \sum_{\lambda=0}^H \mathbb{E} \left[ \sum_{n'=0}^{Q-1} \sum_{l=\Lambda+H}^{n'-\Lambda} s[l]s[l - \Lambda - \lambda] \sum_{n=0}^{Q-1} s[n]s[n - \Lambda - \lambda] \right]
\end{aligned} \tag{53}$$

By utilizing the IID property of the STS sequence, we can easily verify  $\mathbb{E}[\widehat{\text{CIR}}_{l_*}] = 0$  and further obtain the result in (53), where we have used the fact that the expected value is zero whenever  $\lambda' \neq \lambda$  to get the second equality.

By resorting to the IID property of the STS sequence again, we have

$$\mathbb{E} \left[ \widehat{\text{CIR}}_{l_*} \right] = -\frac{\theta \cdot p_R[\epsilon]}{Q^2} \cdot \sum_{\lambda=0}^H \sum_{n'=2\Lambda+H}^{Q-1} (n' - 2\Lambda - H + 1). \tag{54}$$

Accordingly, we can obtain the following asymptotic result:

$$\lim_{Q \rightarrow \infty} \mathbb{E} \left[ \widehat{\text{CIR}}_{l_*} \right] = -\frac{H+1}{2} \theta \cdot p_R[\epsilon]. \tag{55}$$

□

## Appendix G. Azuma-Hoeffding Inequality

The Azuma-Hoeffding inequality and the proof can be found in [27], [28]. We summarize this important inequality here for convenient reference.

**Azuma-Hoeffding Inequality:** *Let  $\{X_0, X_1, \dots\}$  be a martingale, and suppose that there exists two sequence of real numbers  $\{A_0, A_1, \dots\}$  and  $\{B_0, B_1, \dots\}$  such that  $\Pr(A_t \leq X_t - X_{t-1} \leq B_t) = 1, \forall t$ . Then we have,  $\forall \epsilon > 0$ ,*

$$\Pr(X_n - X_0 \geq \epsilon) \leq \exp \left( -\frac{2\epsilon^2}{\sum_{t=1}^n (B_t - A_t)^2} \right). \tag{56}$$

## Appendix H. Sampling Clock at RXD

As shown in Fig. 3, the RXD needs to carry out timing and frequency synchronization to the received signal before processing it further. When there is only the legitimate signal from the TXD in the air, the RXD will acquire the timing and frequency of the TXD. On the other hand, the acquired timing and frequency at the RXD will sync with the attack signal when the transmission from an adversary dominates.

In the case of attack, the RXD will sample and process the received signal according to the clock rate of the attacker upon acquiring timing and frequency. Specifically, the RXD will utilize  $\tilde{T}_c$ , the chip duration from the perspective of the adversary, to determine the sampling period in (6), i.e.,  $T_0 = \tilde{T}_c/\Omega$ . Note that we have  $\tilde{T}_c > T_c$  when the attacker runs a slow clock as described in Section 5.3.

We have looked into the scenario where the clock at the attacker ticks at the same rate as the TXD clock in Section 5.2. In this case, the RXD samples the received attack signal with the clock rate matching that of the TXD. We have further examined how an attacker could take advantage of the clock offsets relative to the TXD in Section 5.3.

## Appendix I. Proof of Proposition 4

*Proof.* Let  $G_n := \sum_{k=0}^{n-1} (\mathbb{E}[x[k]s[k]] - x[k]s[k])$ . We have

$$\begin{aligned}
& \mathbb{E}[G_{n+1}|G_n, G_{n-1}, \dots, G_0] \\
&= G_n + \mathbb{E}[\mathbb{E}[x[n]s[n]] - x[n]s[n]|G_n, G_{n-1}, \dots, G_0] \\
&= G_n + \mathbb{E}[x[n]s[n]] - \mathbb{E}[x[n]s[n]|G_n, G_{n-1}, \dots, G_0] \\
&= G_n + \mathbb{E}[\mathbb{M}(s[n])s[n]] + \mathbb{E}[e[n]s[n]] \\
&\quad - \mathbb{E}[\mathbb{M}(s[n])s[n]|G_n, G_{n-1}, \dots, G_0] \\
&\quad - \mathbb{E}[e[n]s[n]|G_n, G_{n-1}, \dots, G_0] \\
&\stackrel{(a)}{=} G_n - \mathbb{E}[e[n]s[n]|G_n, G_{n-1}, \dots, G_0] \stackrel{(b)}{=} G_n
\end{aligned} \tag{57}$$

where equality (a) utilizes the result in (41) and also the fact that  $s[n]$  is independent of  $\{x[k], s[k]\}_{k < n}$  when the tap  $l_*$  corresponds to the true first path; equality (b) is due to the assumption that the estimation error  $e[n]$  is uncorrelated with  $s[n]$  conditioned on  $\{x[k]\}_{k < n}$  and  $\{s[k]\}_{k < n}$ . Further, we have

$$A_n \leq G_n - G_{n-1} \leq B_n, \tag{58}$$

where

$$A_n = \mathbb{E}[\mathbb{M}(s[n-1])s[n-1]] - 1; \tag{59}$$

$$B_n = \mathbb{E}[\mathbb{M}(s[n-1])s[n-1]] + 1; \tag{60}$$

By resorting to the Azuma-Hoeffding inequality in Appendix G again,  $\forall \epsilon > 0$ , we have

$$\Pr(G_Q \geq \epsilon) \leq \exp\left(-\frac{\epsilon^2}{2Q}\right). \tag{61}$$

The miss detection performance of the detector in (24) is thus given by

$$\begin{aligned}
& \Pr(T(\mathbf{x}) < \gamma) \\
&= \Pr\left(G_Q > \sum_{n=0}^{Q-1} \mathbb{E}[\mathbb{M}(s[n])s[n]] - \sqrt{Q} \cdot \gamma\right) \\
&= \Pr\left(G_Q > Q\bar{C} - \sqrt{Q} \cdot \gamma\right) \\
&\leq \exp\left(-\frac{Q(\bar{C} - \gamma/\sqrt{Q})^2}{2}\right),
\end{aligned} \tag{62}$$

where  $\bar{C}$  is as defined in Proposition 4.  $\square$

## Appendix J. Precursor-Free Pulse

In IEEE 802.15.4 [25], a square-root raised cosine (SRRC) pulse is defined as follows.

$$p_{T, \text{srrc}}(t) = \frac{2}{\pi\sqrt{T_c}} \frac{\cos\left(\frac{3\pi t}{2T_c}\right) + \frac{\sin(0.5\pi t/T_c)}{2t/T_c}}{1 - (2t/T_c)^2}, \tag{63}$$

where  $T_c = 1/499.2 \mu\text{s}$  denotes the length of a chip. The minimum phase decomposition [22] of the SRRC pulse in

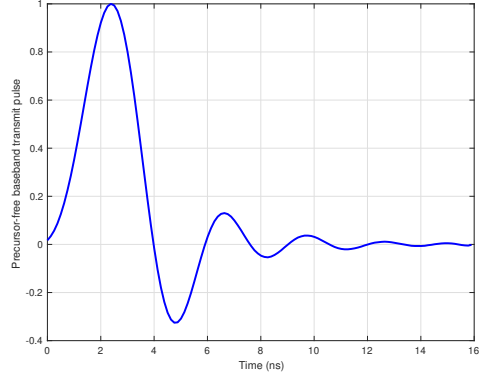


Figure 17. Baseband pulse with minimum precursor energy.

(63) is plotted in Fig. 17. Note that this minimum phase pulse exhibits maximum energy concentration at the pulse beginning.